frontiers | Frontiers in Earth Science

TYPE Original Research
PUBLISHED 08 January 2024
DOI 10.3389/feart.2023.1304402

OPEN ACCESS

EDITED BY
Stanislaw Mazur,
Polish Academy of Sciences, Poland

REVIEWED BY
Liang Qiu,
China University of Geosciences, China
Gaoxue Yang,
Chang'an University, China
Zhao Yang,
Northwest University, China

*CORRESPONDENCE
Hong Chen,
chhzxm8281@163.com

RECEIVED 29 September 2023
ACCEPTED 18 December 2023
PUBLISHED 08 January 2024

CITATION
Chen H, Zhu G-F, Bai H, Cui G-S, Zhang H-H, Mu P-J and Jin Y-J (2024), Late Triassic E-W striking shear zone and its implication on gold mineralization in the Xiaoqinling area, eastern China. *Front. Earth Sci.* 11:1304402. doi: 10.3389/feart.2023.1304402

Late Triassic E-W striking shear zone and its implication on gold mineralization in the Xiaoqinling area, eastern China

Hong Chen[1]*, Gui-Fan Zhu[2], He Bai[3], Guo-Shuai Cui[4], Huan-Huan Zhang[3], Pei-Ji Mu[5] and Yong-Jie Jin[1]

[1]Institute of Geomechanics, Chinese Academy of Geological Sciences, Beijing, China, [2]Cores and Samples Center of Land & Resources, China Geological Survey, Langfang, China, [3]Geological Team No. 6 of Shaanxi Bureau of Geology and Mineral Resources, Xi'an, China, [4]Shaanxi Xinyuan Limited by Share Ltd., Shangluo, China, [5]Institute of Geoscience and Resources, China University of Geosciences, Beijing, China

The Xiaoqinling area is located in the eastern part of the Qinling Orogen and experiences early and late Mesozoic gold mineralization controlled by structural deformation. The relationship between the two stages of mineralization and the orogenic process of the Qinling Orogen is unclear. We investigated the deformation and alteration of E-W striking veins in the Xiaoqinling area. The geometric features revealed that all the veins developed within the E–W-striking Guanyintang brittle–ductile shear zone. The vein was subparallel to the shear zone, dipped at 30°–60°, and had a wave-like appearance. The Guanyintang shear zone underwent three deformation stages: sinistral shearing (D1), dextral thrusting (D2), and sinistral normal faulting (D3). The development of ore-bearing quartz veins was controlled by deformation during D2, and the auriferous pyrite and minor chalcopyrite developed along the shear foliations. Re-Os dating of the molybdenite revealed a well-constrained isochron age of 230.2 ± 2.6 Ma, indicating the E-W striking shear zone developed in Late Triassic. This early Mesozoic shearing deformation in Xiaoqinling represents the early Mesozoic metallogenesis is correlated with the collisional orogeny of the Qinling orogen.

KEYWORDS

Xiaoqinling, gold deposit, E-W striking shear zone, Re-Os dating, Late Triassic

1 Introduction

The Qinling orogen is a collision orogenic belt formed during the Mesozoic collision and collage process between the South and North China blocks (Ratschbacher et al., 2003; Zhang et al., 2004; Dong et al., 2011; Meng and Zhang, 2014; Dong et al., 2016; Dong and Santosh, 2016). Qinling Orogen experienced complex orogenic process in the Mesozoic, which can be divided into collisional shortening in Early-Middle Triassic, intracontinental strike-slip in Late Triassic-Jurassic and extensional depression in Cretaceous (Ratschbacher et al., 2003; Zhang et al., 2004; Hu et al., 2006; Li et al., 2007; Dong et al., 2011, 2016; Dong and Santosh, 2016; Yan et al., 2018a; Yan et al., 2018b), and formed numerous early Mesozoic and late Mesozoic granite bodies (Zhang et al., 2008; Mao et al., 2010; Hu et al., 2012; Zhao et al., 2012; Li et al., 2019). During the intracontinental deformation process, a large number of Mesozoic magmatic hydrothermal gold deposits were formed within the Qinling Orogen (Dong et al., 2016; Xiong et al., 2019; Luo et al., 2020).

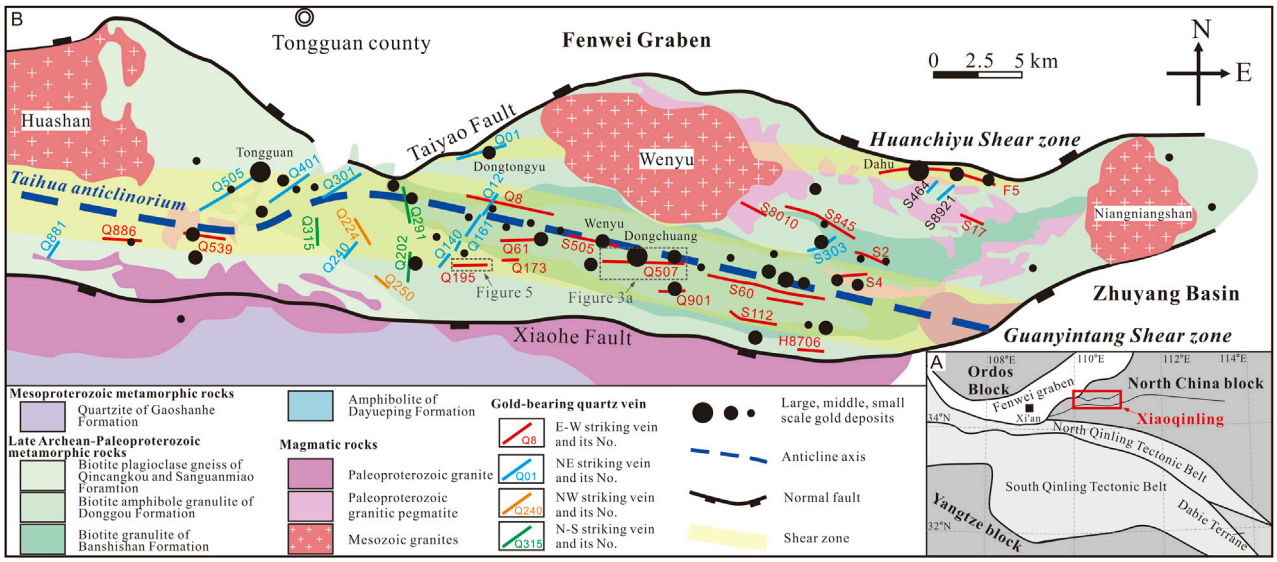

FIGURE 1
(A) Regional tectonic location and **(B)** geological sketch map of the Xiaoqinling area (modified after Jiang et al., 2009; Zhou et al., 2014).

The Xiaoqinling area is located in the northern of Qinling Orogen, and is a part of the southern margin of the North China Block (Ratschbacher et al., 2003; Zhang et al., 2004; Dong et al., 2011; Dong et al., 2016; Dong and Santosh, 2016). Current research suggests that the Xiaoqinling area experienced two stages of tectonic and mineralization events that occurred during the Late Triassic (233–206 Ma) (Li et al., 2007; Li et al., 2011; Jian et al., 2015) and Late Jurassic to Early Cretaceous (144–120 Ma) (Li et al., 2002; Qiang et al., 2013; Hao et al., 2020; Wen et al., 2020). The presence of the Hongtuling gold-molybdenum deposit provides further evidence for the coexistence of these two tectonic and mineralization events during the Late Triassic and Early Cretaceous (Zhao et al., 2019). However, the relationship between the two stages of mineralization in Xiaoqinling and the orogenic process of the Qinling Orogen remains unclear.

The important ore-bearing shear zones discovered in the Xiaoqinling area include the Guanyintang and Huanchiyu shear zones (Jiang et al., 2009; Zhou et al., 2014). The Guanyintang shear zone (GSZ), developed in the core of the Taihua anticline belt, is one of the largest nearly E-W-striking shear zones in the Xiaoqinling area. This shear zone undergoes multiple stages of deformation, such as transpression and transtension, which control the occurrence of orebodies within the shear zone (Feng, 2009; Wang X. C. et al., 2012; Tan et al., 2013; Yan et al., 2013; Tan et al., 2014; Zhang et al., 2015; Han et al., 2016; Wang et al., 2018). Previous research has suggested that the structural deformation controlling the ore body within the shear deformation zone is mainly left-lateral compressive shear deformation (Feng, 2009; Tan et al., 2013), and has undergone four stages of deformation: left-lateral thrusting, mainly thrusting, right-lateral transtension, and mainly extension (Tan et al., 2013). Some studies have also suggested that deformation during the mineralization period is mainly transtension shear deformation (Wang X. C. et al., 2012). Recent structural studies have shown that the formation of ore veins in this shear zone is related to dextral shear deformation (Zhang et al., 2016; Wang et al., 2018).

In this study, we conducted a detailed structural analysis of the E-W striking gold-bearing quartz veins in the Guanyintang shear zone (Tan et al., 2013; Liu et al., 2015). The relationships between shear deformation and quartz veins revealed structural controls during the development of the orebody, which can be used to constrain the mineralization processes associated with the E–W-striking veins in the Xiaoqinling area.

2 Geological setting

The Xiaoqinling area is located in the eastern part of the Qinling Orogen, on the southern edge of the North China Block. It generally extends in a nearly E-W direction (Figure 1A). The Taiyao Fault is located between the north side and the Fenwei Graben, and the Xiaohe Fault is located between the south side and the Zhuyang Basin (Figure 1B; Dong et al., 2011; Fan et al., 2003; Feng, 2009; Li et al., 2020; Zhang et al., 2000, Zhang et al., 2003).

2.1 Strata

The exposed strata in this area are mainly the late Archean-Paleoproterozoic Taihua Group gneiss series, which are sequentially composed of the Dayueping, Banshishan, Donggou, Sanguanmiao, and Qincangkou Formations. The main rock compositions are plagioclase hornblende, biotite plagioclase gneiss, quartzite, and marble (Jia et al., 2016). The Mesoproterozoic Gaoshanhe Formation is exposed on the southern side of the Xiaohe Fault (Figure 1).

2.2 Magmatic rocks

Xiaoqinling has developed magmatic rocks from the Proterozoic to Mesozoic eras (Mao et al., 2010; Hu et al., 2012; Zhao et al., 2012;

Deng and Wang, 2016; Hao et al., 2020; Wen et al., 2020). The Proterozoic magmatic rocks are mainly distributed on the southern side of the tectonic belt and are mainly composed of Xiaohe granite. The Cretaceous granitic magma activity mainly includes the Huashan, Wenyu, and Niangniangshan plutons (Mao et al., 2005; Hao et al., 2020; Wang et al., 2020). This series of magmatic rocks is mainly distributed on the northern side of the tectonic belt, and the lithology is mainly biotite monzogranite and biotite granite.

Simultaneously, a large number of mafic veins and granite pegmatites have developed in the region, among which granitic pegmatites are mainly produced in the form of veins and intrude only along the boundary of the Wenyu pluton to the northeast (Wang et al., 2008; Wang et al., 2023). These veins have a certain spatial correlation with gold-bearing quartz veins, such as Q291 and Q292 near Taiyao (Figure 1).

2.3 Structural characteristics

There are obvious folds in the Xiaoqinling gold deposit area, with the Taihua anticline near the E-W direction as the main body (Zhang et al., 2000; Mao et al., 2002; Fan et al., 2003; Feng, 2009; Liu et al., 2015). This anticline is located on the south side of the Wenyu Pluton and extends from west to east along gold deposits, such as Tongguan, Haochayu, Wenyu, and Jindongcha (Figure 1B). A large number of mineral stretching lineations have developed nearly parallel to the anticline hinge, indicating the development of a metamorphic core complex in the Early Cretaceous (Zhang et al., 2000; Li et al., 2020).

Along the core of the Taihua anticline, a large shear zone with a width of approximately 5 km has developed, namely the Guanyintang shear zone (also known as the Dayueping shear zone) (Jiang et al., 2009; Zhou et al., 2014). The shear zone is generally in a nearly E-W direction and mainly develops within the Dayueping Formation of the Taihua Group in the core of the Taihua anticline. The strike was mainly 100°–110°, dipping southward with a dip angle of approximately 50°. Thrust deformation characteristics with strike-slip components within the shear zone are evident (Wang X. C. et al., 2012; Tan et al., 2013). Large ore veins are exposed along this shear zone, the most typical being veinss such as Q8 and Q507, which form large-scale ore-bodies (Figure 1).

There are several medium-to high-temperature hydrothermal quartz vein-hosted gold deposits in the Xiaoqinling area (Jiang, 2000; Fan et al., 2003; Feng, 2009; Wu et al., 2012; Xu et al., 2013). The distribution and enrichment of veins are related to their tectonic settings (Fang et al., 2000; Yan et al., 2013). The quartz veins in the Xiaoqinling area can be divided into four groups (E–W, NW–SE, NE–SW, and N–S) based on their dominant occurrences (Chen et al., 2021). The thickest and longest veins typically strike E–W and comprise the most important part of the Xiaoqinling area because of their high ore grades (Wang T. et al., 2012; Deng and Wang, 2016). These E–W-striking veins commonly occur in brittle–ductile shear zones, which control the shape and distribution of auriferous veins and the occurrence of ore minerals (Chao, 1989; Tan et al., 2013).

The Xiaohe and Taiyao faults were initially extensional structures (Zhang and Zheng, 1999; Zhang et al., 2003) that were reactivated as normal faults during the Cenozoic. The Xiaohe Fault controls the distribution of nearby secondary faults, as well as the development and scale of gold-bearing quartz veins. Hundreds of gold deposits are located within the brittle–ductile shear zones that strike dominantly E–W, NE–SW, NW–SE, and N–S (Chao, 1989; Wang X. C. et al., 2012; Zhang et al., 2015), but mainly in the Guanyintang shear zone, which strikes WNW–ESE, dips to the south, and extends for approximately 18 km (Figure 1B).

2.4 Metallogenic characteristics

Previous studies have divided mineralization in the Xiaoqinling area into four stages: pyrite–quartz veins (I), quartz–pyrite veins (II), sulfur–polymetallic–quartz veins (III), and quartz–carbonate veins (IV) (Figure 2; Jiang, 2000; Tan et al., 2013; Xu J. H. et al., 1998). Regarding the mineralization and gold precipitation mechanisms of quartz vein-type gold deposits, previous studies based on geochemistry and fluid inclusions in mineral deposits have shown that gold usually occurs in pyrite, chalcopyrite, galena, and sphalerite (Figure 2H) in the form of inclusions or veins formed in phases II and III; 90% of the gold occurs in pyrite and chalcopyrite (Figure 2I; Liu et al., 2015; Tan et al., 2012).

For the mineralization time, based on Re-Os and Ar-Ar dating, some researchers have suggested a late Mesozoic age of 143–118 Ma (Chao, 1989; Li et al., 1998; Li et al., 2002; Wang et al., 2002; Li et al., 2007; Chen et al., 2009), whereas others have suggested an early Mesozoic age of 233–206 Ma (Li et al., 2007; Li et al., 2008, 2011; Lu et al., 2008; Jiang et al., 2009; Chen, 2010; Jian et al., 2015; Deng and Wang, 2016; Cao et al., 2017).

3 Shear deformation of the gold-bearing quartz veins

We analyzed the structural deformation characteristics of five ore veins at different structural segments within the shear zone, including Q507, Q195, Q8, Q539, and Q886, from east to west (Figure 1).

3.1 Vein Q507

Vein Q507 is located in the eastern segment of the GSZ, at the border between Shaanxi Province and Henan Province at elevations of 1,850–2,165 m, and is one of the most typical ore-bearing quartz veins in the Xiaoqinling area (Figures 3A, B; Tan et al., 2013). It occurs within the core of the Taihua anticlinorium (Figure 1). At the surface, the vein strikes 275°–285° and dips 30°–65° to the south. Exploration drilling results (maximum depth = 820 m) suggest that the vein striked WNW–ESE (270°–290°), dipped 35°–55° to the south, and had a length up to 1,450 m. The quartz veins were 0.5–3.5 m wide. Quartz occurred as veins and lenticular and wave-like bodies controlled by the development of mylonite, schist, and cataclasite within the shear zone.

Vein Q507 in the Chen'er gold deposit can be divided into western and eastern ore-bodies (Figure 3B). Here, we present a structural analysis of four levels at elevations of 1,348, 1,430, 1,510, and 1,550 m in the east (Figure 3C) and five levels at elevations of 850, 943, 1,023, 1,103, and 1,420 m in the west (Figure 3D).

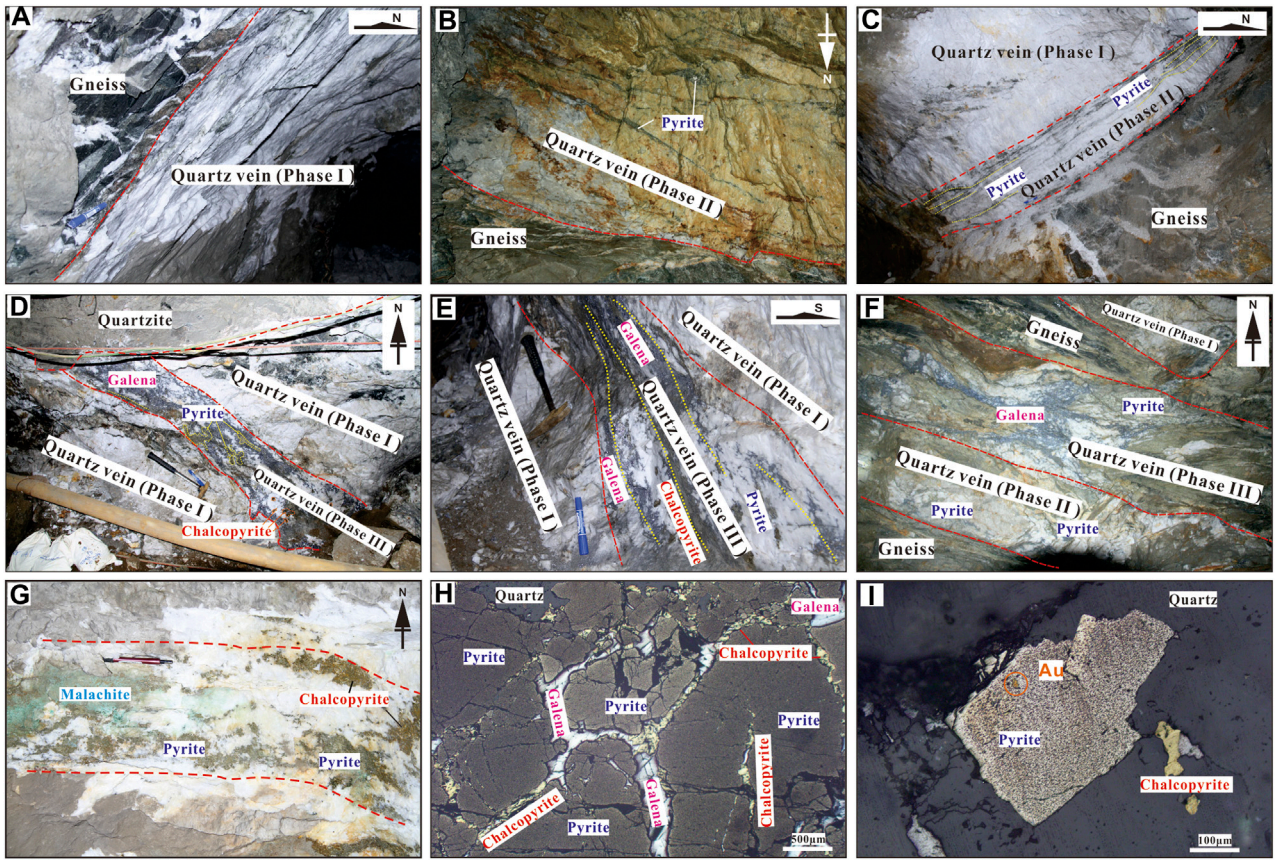

FIGURE 2
Mineralization within E-W striking veins. **(A)** Non-mineralized quartz veins (Phase I) in Q886; **(B)** Pyrite-bearing quartz veins (Phase II) in Q8; **(C)** Non-mineralized quartz veins (Phase I) and pyrite-bearing quartz veins (Phase II) in Q507; **(D)** Phase I and sulfur polymetallic quartz veins (Phase III) in Q507; **(E)** Galena distributed along foliations in Q507; **(F)** Three-phases quartz veins in Q61; **(G)** Agglomerated pyrite and chalcopyrite mineralization in Q507; **(H)** Chalcopyrite and galena fill in the cracks in the pyrite in Q507; **(I)** Natural gold in pyrite in Q507.

Within the eastern ore body, the shear zone striked dominantly 275°–295° and dipped 40°–60° to the south, with a small section that dipped more steeply (Figure 3C). Quartz veins are typically subparallel to or shallower than the shear zone. In all five analyzed levels across the western ore body, the shear zone and vein had similar orientations, striking 295° and dipping 35°–45° to the south (Figure 3D). The shear zone and vein were thin, and the shear zone dipped steeply (Figures 3C, D).

The eastern ore-body exhibited a wave-like geometry and showed significant changes in shape within each level. In contrast to the western ore-body, the eastern ore-body exhibited variations in strike. The shape and thickness of the vein varies at some levels, whereas in others (e.g., 1,510 m), the thickness of the vein did not vary despite changes in its shape and the development of branching and compound structures (Figure 4A). Most ores are hosted in thick milky-white quartz veins (Figure 4A) and display complex thin features. The boundaries of the branching veins striked 260° and dip 40° to the south. The southern boundary of the quartz vein is a fracture surface that strikes 285° and dips 65° to the south. In general, vein thickness gradually increased from west to east. For example, at a level of 1,430 m, the shear zone changed its orientation from striking 205° and dipping 53° to striking 195° and dipping 65°, and its thickness increased from 1 to 2 m to more than 3 m (Figure 4B). A relatively thin NE-trending shear zone was observed at this level (Figure 4B). These NE-trending quartz veins striked at 225° and a lens of quartz occurred above the quartz vein, indicating sinistral slip and suggesting that the NE-trending veins were controlled by sinistral deformation during mineralization (Figure 4C).

At a depth of 1,510 m, mineralization occurs within lenticular bodies that dip at a shallower angle than the quartz vein boundaries (Figure 4D), which is consistent with thrusting during metallogenesis. At the northern end of the quartz vein, a mineralized late-stage shear zone cuts early quartz veins with a strike of 285° and a dip of 60° to the south (Figure 4A). Drag folds occurred in the hanging wall of the shear zone at 850 m (Figure 4E), whereas mineralization within the quartz veins was observed close to the boundaries between the quartz vein and the host rock. At 1,550 m, the felsic wall rocks were mylonitized, striked at 280°, and dipped at 53° to the south. Microscopic observations revealed rotated sigma grains and fractures within microcline grains (Figure 4F), indicating thrust deformation. At 1,430 m, samples were collected from the NE-striking quartz veins (strike = 250°, dip = 50° to the SE). The mica grains were strongly aligned and formed C–C′ fabrics (Figure 4G). Pyrite filled the cracks, the orientation of which indicates that the shear zone underwent thrust deformation. These observations are consistent with thrust deformation.

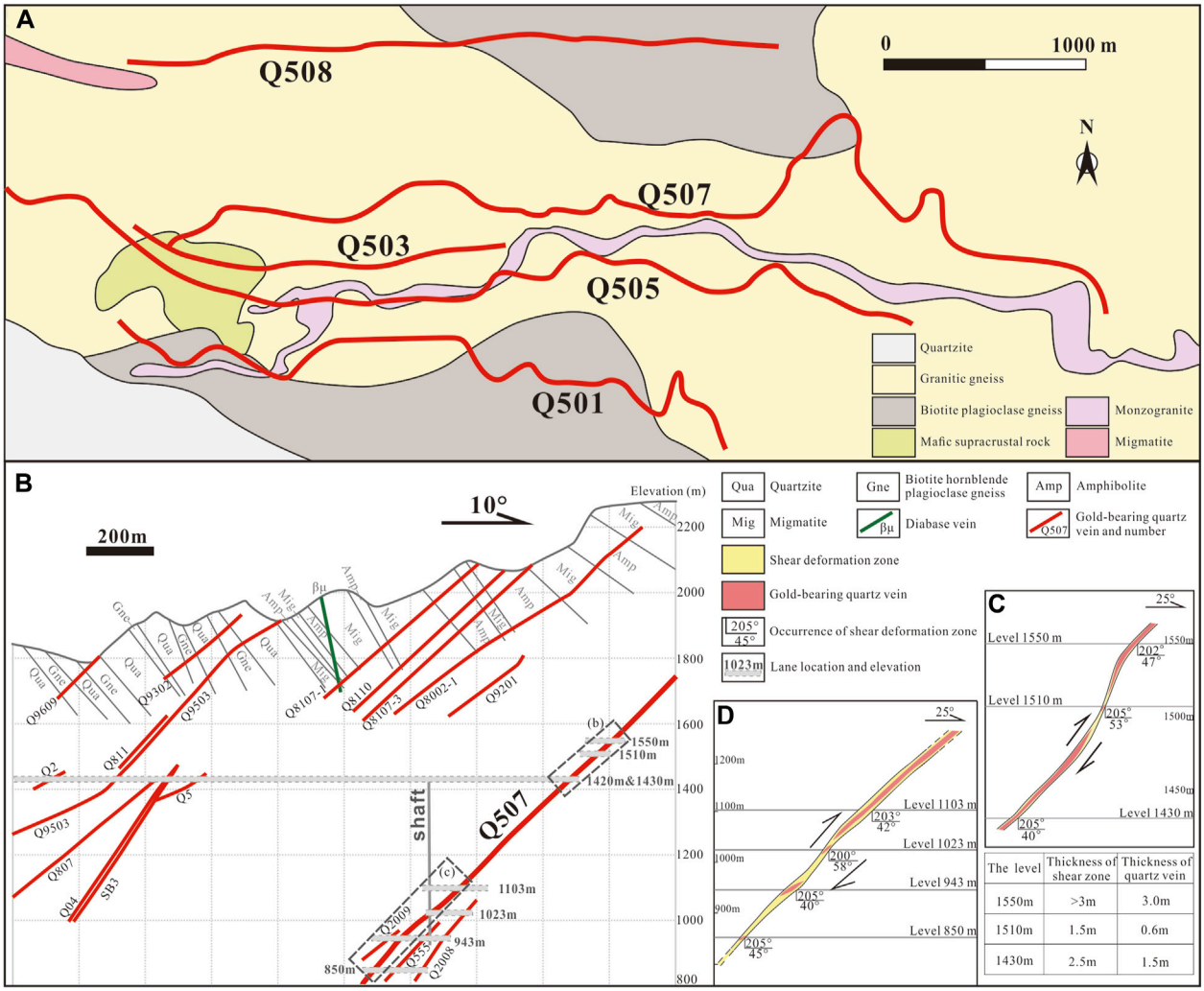

FIGURE 3
(A) Geological sketch map of the Q507 gold deposit (modified after Tan et al., 2013); **(B)** Cross-section showing the vertical distribution of Q507 in the Chen'er gold deposit (modified after Tan et al., 2012); **(C)** Sketch showing a vertical projection of the east ore body; **(D)** Sketch showing a vertical projection of the west ore body.

This vein exhibited dextral deformation during the primary phase of metallogenesis (F2) (Figure 4A). During this period, milky-white foliated barren quartz veins developed, and ore-bearing hydrothermal fluid was concentrated along the structural surface. Mineralization within the quartz veins striked 275° at a level 1,430 m, consistent with dextral shear (Figure 4H). C–C′ fabrics, which comprised early ore fissures or quartz veins (F1) and a shear zone boundary, were observed at several levels, indicating dextral shear (Figure 4I). At a level of 1,510 m, the host rock was a mylonitic schist that striked 280° and dipped at 45° to the south. The mica grains were elongated and showed a preferred orientation, forming an S–C–C′ fabric consistent with dextral thrust deformation (Figure 4J).

At 1,023 m, late calcite–quartz veins developed along the tensional shear fractures, indicating that the hanging wall was downthrown (F2) (Figure 4K). Furthermore, striations indicating sinistral slip were observed at several locations within the shear zone and along the boundary with the host rock, which reversed the E-W compressive stress field (Figure 4L). Many late-stage en echelon calcite–quartz veins were observed within the shear zone and host rock, and sinistral motion (F2) was recorded (Figure 4M).

3.2 Vein Q195

The Q195 vein is situated in the center of the GSZ near the core of the Taihua anticline (Figure 1). This vein predominantly trends in the E-W direction and spans approximately 1,350 m. It is characterized by the presence of three quartz vein lenses that display disseminated and stockwork-style polymetallic mineralization (Figure 5). The veins are located within a shear zone that generally exhibits a gentle southward dip at 175° with a low angle of 35°.

The shear deformation zone predominantly consisted of green schists and quartz veins. These quartz veins intruded along the foliation and maintained a consistent orientation with the foliation

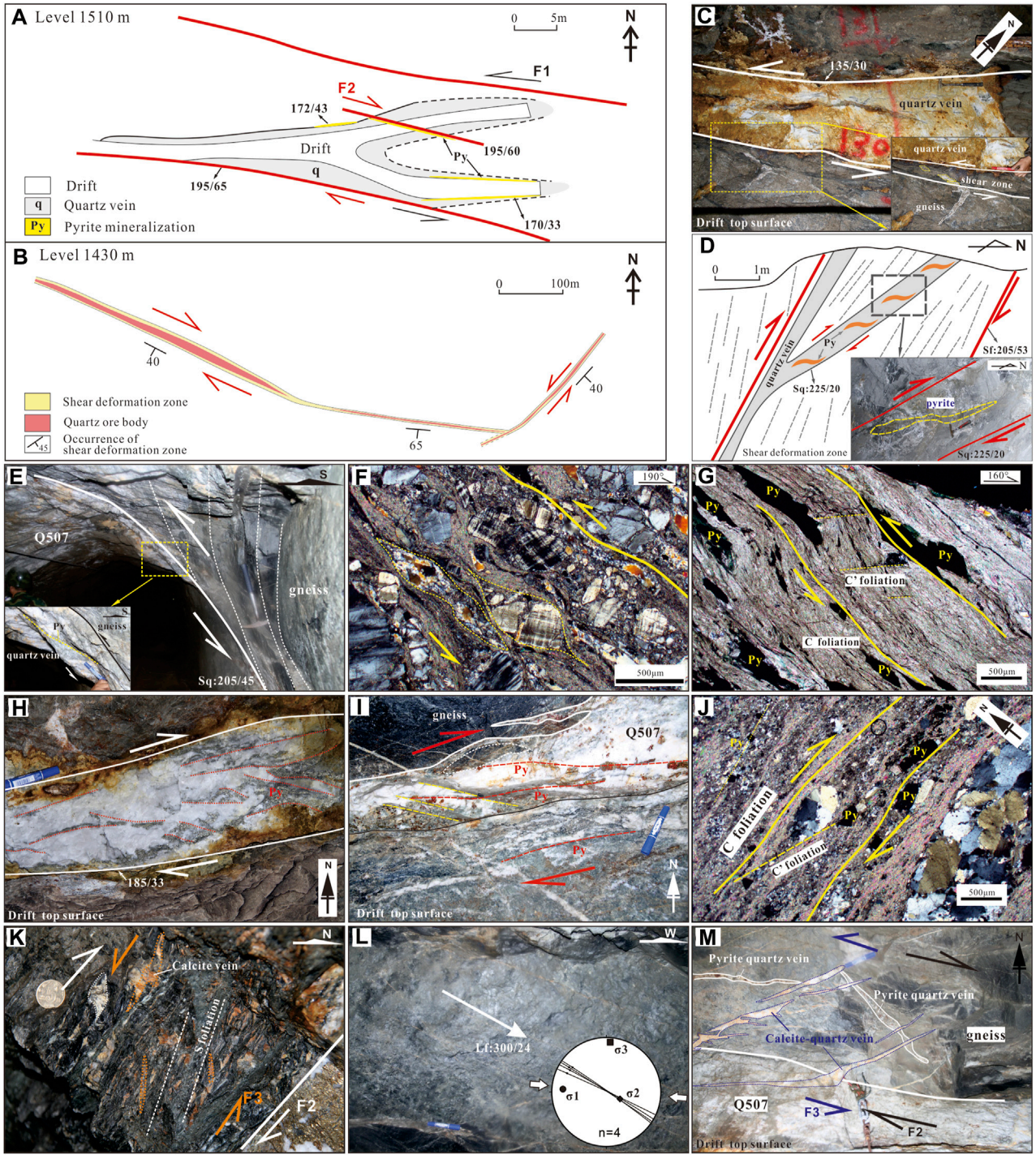

FIGURE 4
Deformation structures that formed during metallogenesis in Q507 at eastern segment of GSZ. **(A)** Planar features of the vein at 1,510 m; **(B)** Planar features of the vein at 1,430 m; **(C)** Quartz vein striking 225° and quartz lenses in host rock recording sinistral deformation; **(D)** Sketch showing the occurrence of quartz veins and lens of pyrite recording the thrust deformation; **(E)** Drag fold close to the shear zone boundary and mineralized belts within quartz veins; **(F)** C−C′ fabric and rotated grains indicating thrust deformation (cross-polarized light); **(G)** C−C′ fabric indicating thrust motion (plane-polarized light); **(H)** Oblique mineralization recording dextral slip within a quartz vein striking 275°; **(I)** Ore-bearing fissures and shear zone boundary forming a C−C′ fabric; **(J)** S-C-C′ fabric indicating dextral deformation (cross-polarized light); **(K)** Primary foliation (S) and quartz lenses with late-stage calcite−quartz veins recording normal-faulting displacement (F3); **(L)** Striation indicating sinistral normal faulting and the reversed stress field; **(M)** Acute angle between the ore-bearing quartz veins and shear bands. Py-pyrite; Sq: boundary of the quartz vein; Sf: fault plane; Lf: striation or lineation; Sg: gneissosity.

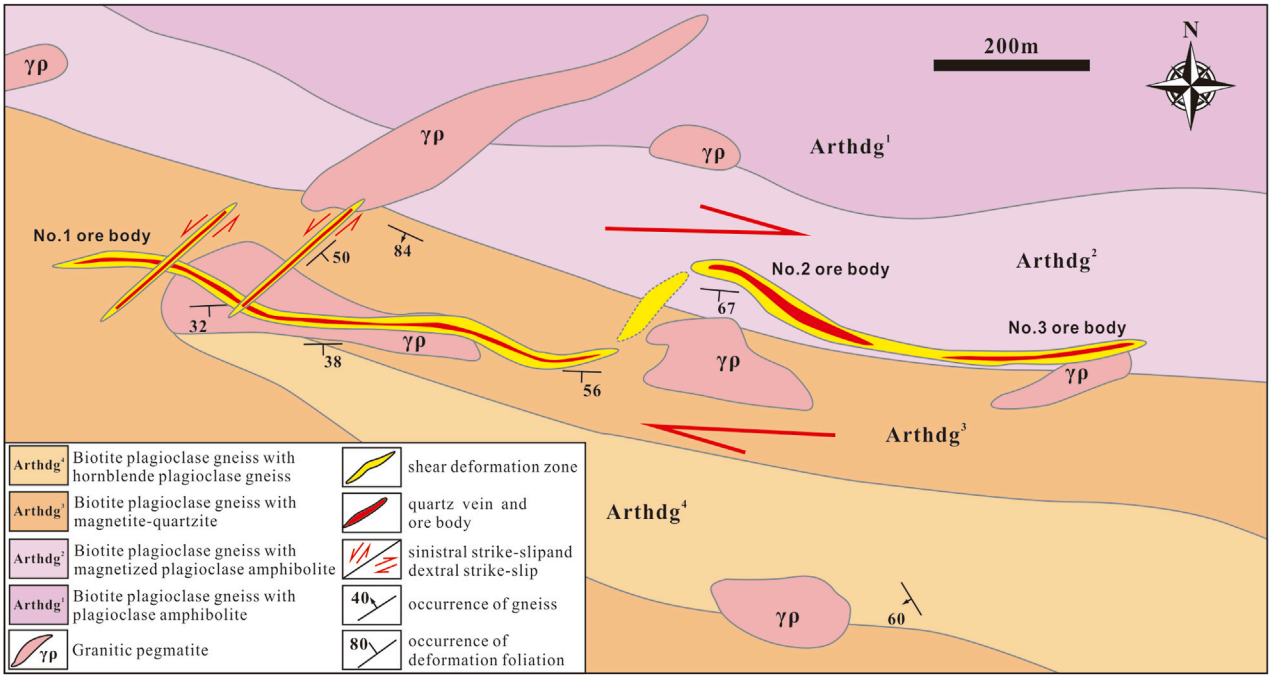

FIGURE 5
Geological sketch map and distribution characteristics of Q195 at the central segment of GSZ.

in the adjacent rock (Figure 6A). Within this deformation zone, the typical width of quartz veins was approximately 40 cm. However, in certain regions, these quartz veins can be narrower, measuring only 5–10 cm or completely absent (Figure 6B). The structural characteristics within the remaining vein bodies and deformation zone revealed that the primary deformation in this region was marked by right-lateral thrust shearing (Figures 6B–D). The primary structural alignment within this zone extended eastward and inclined at an approximate angle of 45°. This zone displayed the features of oblique shear deformation. On the exposed surface at the top of this deformation zone, the neighboring rock demonstrated distinct shear deformation, characterized by mylonitic foliation, σ-type porphyroblasts and structural cleavage, which signify a right-lateral shear deformation pattern (Figure 6E).

Furthermore, there was a set of nearly parallel SE-trending vein bodies at both the surface and vein levels. The overall orientation within the deformation zone was approximately trending to 130° with dip angle of 45° (Figures 5, 6F, G). The SE-trending deformation zone cut across the S-dipping deformation zone of Q195. There were evident vein offsets and tensional folds within the S-dipping deformation zone (Figures 6H, I), indicating a distinct left-lateral movement. The structural relationship between the two sets of deformation zones indicates that the S-dipping deformation zone formed earlier, whereas the SE-trending deformation zone formed slightly later. The structural stress field inferred from the fault slip inversion showed that the principal stress directions for both zones were oriented in a NW-SE direction. However, there were differences in the stress mechanisms (Figures 6D, F). In the case of the near E-W striking deformation, shear strain predominated, whereas in the NE-striking deformation, is shortening strain prevailed.

3.3 Vein Q8

The Q8 vein is located in the middle section of the GSZ, on the northern flank of the Taihua Anticline. It has a total surface exposure length of approximately 4430 m and varies in thickness from 0.15 to 4.15 m. The shear deformation zone, in which this vein is situated, generally trends in the E-W direction, with an overall trend of 182° and a dip angle of 50°. In some localized areas, it may exhibit NNW and NNE trends, with moderate dip angles ranging from 40° to 50° (Figure 7A). Within the deformation zone, the development of lens-shaped quartz veins is a prominent feature, with the thickest veins reaching approximately 2 m, typically averaging approximately 0.5 m in thickness. These quartz veins generally follow shear foliation (Figure 7A).

Within this deformation zone, there is clear evidence of thrust deformation resulting in distinct mineral stretching lineations. These lineations plunged to 170°–195° with angle of 40°–50°, indicating brittle-ductile shear deformation (Figures 7B, C). Additionally, within the shear zone, there are bands of pyrite-quartz veins that intersect the shear foliation at small angles trending to 213° and dipping at 42° (Figure 7B). Furthermore, interleaved lenses of calcite-quartz veins were arranged in en echelon patterns (Figure 7D). The boundaries of the pyrite veins exhibited banded filling (Figure 7E), which revealed right-lateral shear deformation. In the host rock beneath the quartz vein, there is evidence of drag folds and extensional fractures filled with quartz veins. Within the quartz veins, aligned bands of pyrite were observed (Figure 7F). These observations collectively indicate that the ore-forming process of the Q8 vein was related to right-lateral thrust deformation.

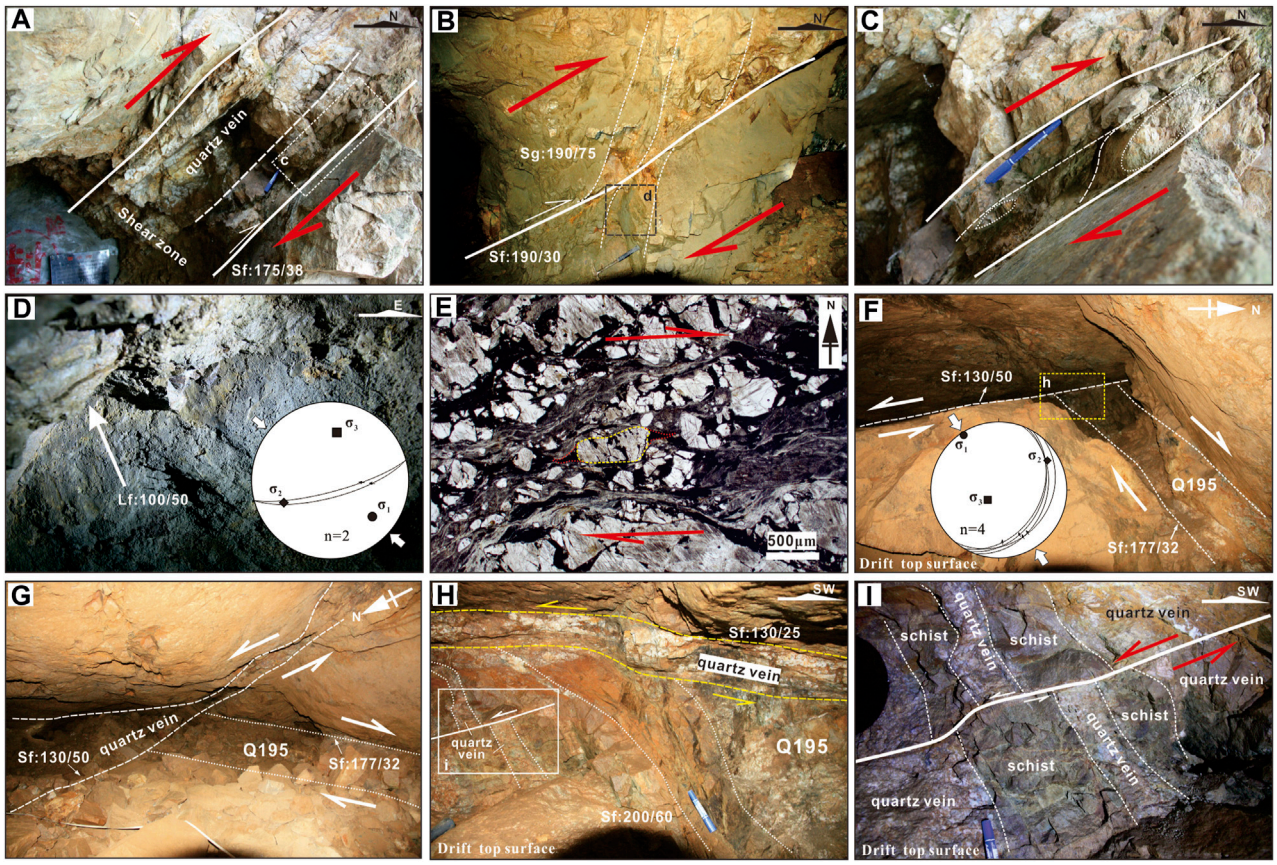

FIGURE 6
Deformation structures formed during metallogenesis in Q195 at central segment of GSZ. **(A)** Quartz veins intruded along the shear foliation; **(B)** Drag fold formed by gneissosity indicating thrust deformation; **(C)** Quartz lenses in the shear zone; **(D)** Striation on the fault plane indicating thrust deformation and reversed stress field; **(E)** Mylonitic foliation, σ-type porphyroblasts indicating right-lateral shearing; **(F–H)** NE striking vein offset Q195; **(I)** Quartz vein left-lateral offset by NE-striking fault.

3.4 Vein Q539

Q539 is located in the western segment of the shear zone and is characterized by the development of thick quartz veins, with the thickest veins reaching up to 5 m. The vein boundaries trends at 190° with a dip angle of 40° (Figure 8A). The structural foliation of the shear deformation zone where this vein is situated trends to 195° and contains numerous structural lenses, indicating characteristics of thrust deformation (Figure 8A). Along with structural foliation, galena, chalcopyrite, pyrite, and other sulfides occur (Figure 8B). Additionally, molybdenite can be observed along the NE-striking structural foliation, trending to 130° with a dip angle of 30°. The NE-striking and S-trending structural foliations formed the C-C′ fabric, which indicated thrust deformation (Figures 8C, D). Molybdenite appears as thin sheets along the structural foliations (Figure 8E), which indicated that its formation is related to thrust deformation.

3.5 Vein Q886

The Q886 vein is situated in the westernmost extremity of the GSZ and extends over a surface length of approximately 1 km. Within the shear deformation zone where this vein was found, the thickness varies from 0.20 to 3.10 m. This ore-bearing shear zone exhibited a continuous distribution and was composed of structurally altered rocks, schists, and quartz veins. Based on field observations conducted at the level of the Q886 vein, it was found that the shear zone predominantly extended in the E-W direction, trending to 180° with dip angle of 40°. Multiple lens-shaped quartz vein bodies, arranged in a sub-parallel fashion, developed within this shear zone (Figure 9A). Additionally, within the deformation zone, there were quartz veins with thicknesses of up to 2 m, and their boundaries trending to 145° with dip angle of 40°.

In the host rocks, both above and below the E-W striking quartz veins, drag folds were formed near the shear deformation zone (Figures 9B, C). Beneath the shear zone, horizontally-oriented lens-shaped quartz veins formed in an extensional environment (Figure 9D), indicating thrust deformation characteristics. In the plane view, macroscopic S-C structures were visible within the shear zone (Figure 9E), and granitic pegmatite veins formed asymmetric folds (Figure 9F), collectively indicating features of right-lateral strike-slip deformation. Inside the tunnel at the 1,600 m level of the Q886 vein, there was a banded lamprophyre vein that had been offset by approximately 2 m within the shear zone (Figure 9G). At the boundaries and within the quartz veins, pyrite and galena developed along the shear foliations and fractures. Additionally, pyrite was often filled along the C′ foliation, and pyrite

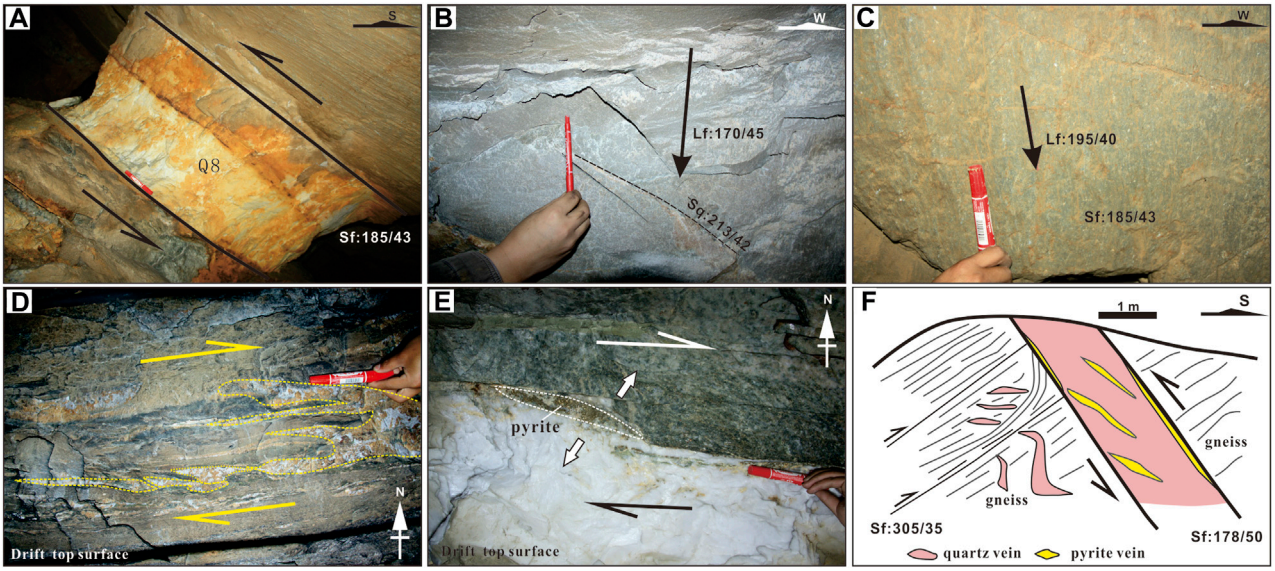

FIGURE 7
Deformation structures that formed during metallogenesis in Q8 at central segment of GSZ. **(A)** Occurrence of the quartz vein in shear zone; **(B)** Stretching lineation and occurrence of pyrite-quartz veins; **(C)** Stretching lineation on the shear foliation; **(D)** Lenses of calcite-quartz veins arranged in en echelon patterns; **(E)** Pyrite veins filled in the tensile fracture; **(F)** Sketch showing the occurrence of quartz veins and lens of pyrite recording the thrust deformation.

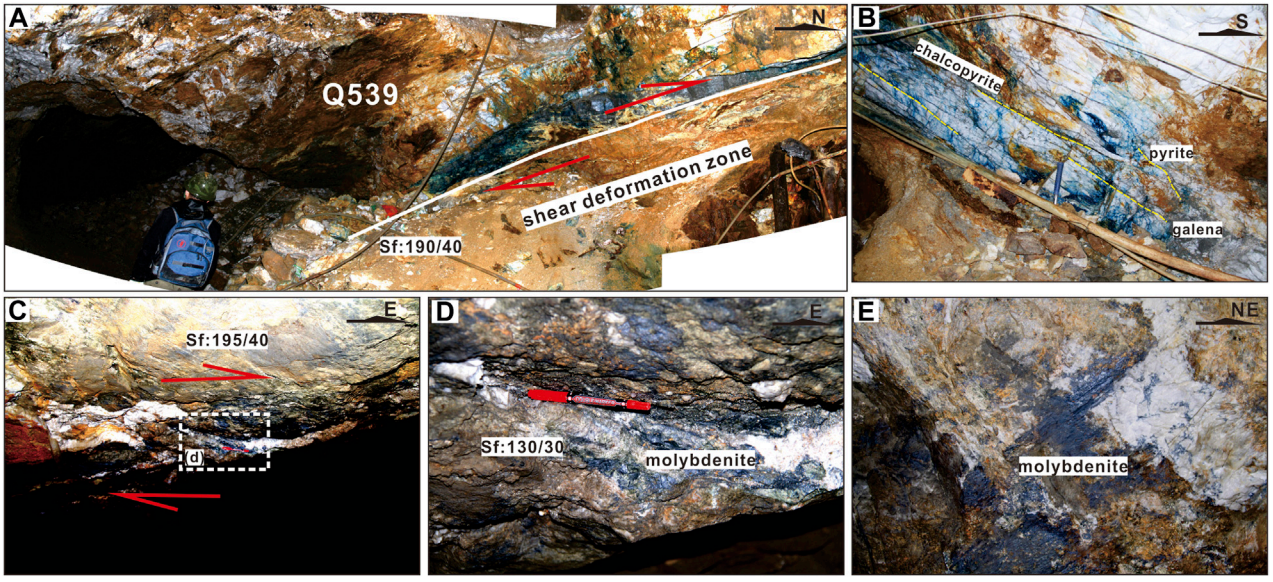

FIGURE 8
Deformation structures that formed during metallogenesis in Q539 at western segment of GSZ. **(A)** Occurrence of the quartz vein in shear zone; **(B)** Galena, chalcopyrite, pyrite, and other sulfides developed along the foliation; **(C,D)** Molybdenite developed along the NNE-trending foliation; **(E)** Occurrence of the molybdenite for dating.

mineralization was observed in the side branches, indicating an association between the ore-forming process and right-lateral shear deformation (Figure 9H).

Late-stage normal fault striation were visible on the main boundary surface of this shear zone. The fault plane was trending to 170° with a dip angle of 56°, while the striation plunged to 143° at 45° (Figure 9I), indicating characteristics of left-lateral normal faulting. Additionally, within the shear zone, the en echelon arrays of calcite-quartz veins trended to 100° with a low angle of 10° (Figure 9J), suggesting left-lateral movement.

In summary, the shear deformation zone where the Q886 vein is situated has experienced at least two superimposed phases of

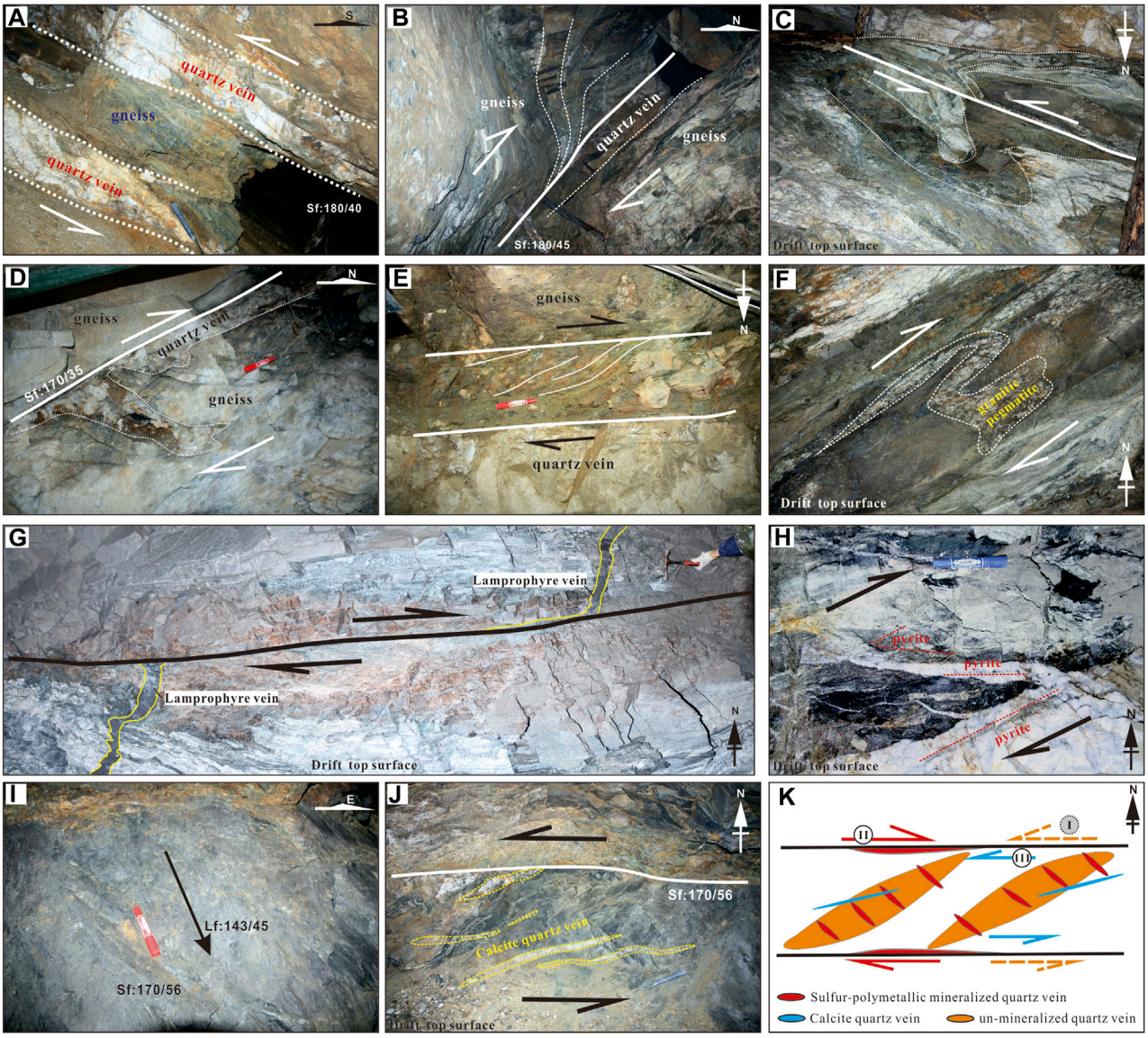

FIGURE 9
Deformation structures that formed during metallogenesis in Q886 at western segment of GSZ. **(A)** Occurrence of the parallel quartz veins in shear zone; **(B)** and **(C)** Drag folds forming by the gneissosity indicating thrust deformation; **(D)** Lens-shaped quartz veins indicating thrust deformation; **(E)** S-C structures within the shear zone indicating dextral strike-slip; **(F)** Asymmetric folds formed by the granitic pegmatite veins; **(G)** Lamprophyre vein right-lateral offset; **(H)** Pyrite filling along the C′ foliation; **(I)** Striation indicating sinistral normal faulting; **(J)** Calcite quartz veins indicating sinistral strike-slip; **(K)** Sketch showing the superimposed phases of deformation and mineralization for Q886.

deformation and mineralization (Figure 9K). An early phase of right-lateral thrust deformation (Phase II) represents the structural deformation of the ore-forming period. It is characterized by the development of pyrite and chalcopyrite along the structural foliation, resulting in banded pyrite mineralization. This phase exhibited the characteristics of late-stage structural hydrothermal filling and caused significant drag-fold deformation in the surrounding rocks. A later phase of left-lateral normal faulting (Phase III) occurred, which often reactivated along the earlier structural surfaces but did not significantly alter the overall characteristics of the vein. In addition, within the deformation zone, the E-W striking quartz veins notably modified the thick NNE-striking quartz vein lenses. These two sets of veins differed in their occurrence and mineralization characteristics, suggesting the possibility of an even earlier phase of left-lateral thrust deformation (Phase I).

4 Molybdenite Re-Os dating

4.1 Samples

Seven molybdenite samples were collected from the NE-striking and S-trending structural foliation in Q539 ore veins for the Re-Os dating (Figure 8). All molybdenite samples used for dating were subjected to indoor pollution-free crushing and sorting, and purified

TABLE1 Re-Os isotopic data for molybdenite from Q539 quartz vein.

Sample no.	Weight (g)	Re (ppb)		Common Os (ppb)		^{187}Re (ppb)		^{187}Os (ppb)		Model age (Ma)	
		Measured	±2σ	Measured	±2σ	Measured	±2σ	Measured	±2σ	Measured	±2σ
XQC08-1	0.02171	21,145	282	0.0532	0.0440	13,290	177	51.03	0.42	230.0	4.3
XQC08-2	0.01531	21,815	257	0.0198	0.0122	13,711	161	52.72	0.33	230.4	3.8
XQC08-3	0.02092	1999	22	0.4336	0.0236	1,256	14	4.861	0.035	231.8	3.8
XQC08-6	0.02079	2,215	27	0.0222	0.0017	1,392	17	5.272	0.042	226.9	4.0
XQC08-7	0.03993	4,603	33	0.0307	0.0154	2,893	20	10.95	0.07	226.7	3.1
XQC08-8	0.03010	19,221	192	0.0111	0.0003	12,081	121	46.18	0.31	229.0	3.6
XQC08-15	0.05023	8,475	94	0.5883	0.0146	5,327	59	20.64	0.12	232.2	3.7

under binocular lenses to obtain molybdenite samples with a purity greater than 99%. Descriptions of the molybdenite samples are listed in Table 1.

4.2 Methods

Re–Os isotope analyses were performed at the National Research Center of Geoanalysis, Chinese Academy of Geological Sciences, China. The detailed procedures are described in Du et al. (2004) and Leng et al. (2013). Osmium was isolated and purified from the acidic solution using a 50% HBr solution and microdistillation. The Re from the Os-extracted solution was separated via NaOH–acetone extraction. The compositions of the Re and Os isotopes were measured using N-TIMS (Triton Plus). The analytical reliability was tested by analyzing the certified reference materials JCBY. The model Re-Os age was calculated using the equation [$t = \ln(^{187}Os/^{187}Re + 1)/\lambda$, using the decay constant (λ) of $1.666e^{-11}$ a^{-1} (Smoliar et al., 1996). Uncertainties were determined using the uncertainty in weighing the sample and tracer solution, calibration of the tracer solution, mass spectrometry measurements, and blank values. The common Re $^{185}Re/^{187}Re$=0.59738 was used as the external standard for the mass fractionation correction of Re isotopes, and $^{192}Os/^{188}Os$=3.0827 was used as the internal standard iteration method for the mass fractionation correction of Os. All uncertainties are presented at the 2σ absolute level. Concordia diagrams and weighted mean calculations were performed using the Isoplot software (ver. 4.15) (Ludwig, 2011).

4.3 Results

The seven molybdenite samples contained 1999–21815 ppb Re and 4.861–52.72 ppb ^{187}Os (Table 1). Regression of ^{187}Re and ^{187}Os contents defines a well-constrained isochron age of 230.2 ± 2.6 Ma, with initial ^{187}Os = −0.04 ± 0.18 ppb (MSWD =3.1; Figure 10A). The calculated model ages ranged from 226.7 ± 3.1 Ma (2σ) to 232.2 ± 3.7 Ma (2σ), with a weighted average age of 229.4 ± 2.1 Ma (2σ, MSWD =1.5, n = 7, Figure 10B). The isochron age was similar to the weighted average model age (Figure 10), the measured initial ^{187}Os met the calculation conditions for the age of the Re-Os isotope system model, and the data were reliable.

5 Discussion

According to previous studies, in the Neoarchean-Paleozoic, the Xiaoqinling area experienced a continental crust growth event on the periphery of the original continental core, accompanied by the re-construction of ancient continental crust material (Hu et al., 2013). Subsequently, the Xiaoqinling area was affected by multistage tectonic evolution, forming a series of folds and shear zones. Since the early Mesozoic period, the collision between the Yangtze and North China blocks, the South Qinling Block, and the North China Block have fully integrated the Qinling Mountains, creating a geotectonic pattern of a multi-terrain collage (Meng and Zhang, 2014; Tan et al., 2014; Dong and Santosh, 2016). The late Mesozoic period was an important stage of extensional tectonic evolution in eastern China, producing a series of metamorphic core complexes and associated gold deposits (Zhang et al., 2000; Li et al., 2012a; Li et al., 2012b; Zhu et al., 2015; Deng and Wang, 2016; He et al., 2016). Among them, gold mineralization is closely related to the role of hydrothermal fluids in the intracontinental orogeny at the end of the Triassic period. The Xiaoqinling gold field is an important metallogenic series.

5.1 Structural deformation in E-W striking shear zone

The E–W-striking shear zone in the Xiaoqinling area dips moderately toward the south and is controlled by thrust, sinistral, and dextral deformations (Tan et al., 2014). The structural characteristics of different segments of E-W striking GSZ in the Xiaoqinling area have been studied. All the main bodies of gold-bearing quartz veins in this shear zone trended to south at angle of 30°–50°. These quartz veins were typically arranged in en echelon patterns in the form of lens-shaped bodies and intersected the shear zones in parallel or at shallow angles (Figures 3–9).

Analysis of the structural deformation characteristics of different structural segments of the GSZ shear zone indicated that the E-W striking shear deformation zone had undergone a superimposition of dextral thrust deformation (D2) and sinistral normal faulting deformation (D3). Within the shear zone, the development of features such as drag folds (Figures 4E, 6B, 9B), S-C-C′ structures (Figures 4G, J, 9E), rotated porphyroclasts

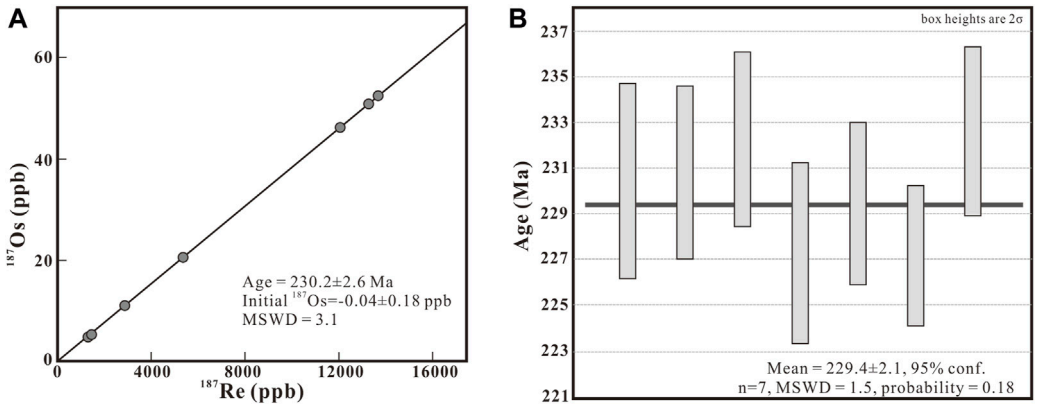

FIGURE 10
(A) Re-Os isochron and **(B)** weighted average model age diagrams for molybdenite from the Q539.

(Figures 4F, 6E), asymmetric folds (Figure 9F), and en echelon arrangements of quartz veins (Figure 4D; Figure 5), suggest that right-lateral thrust deformation was predominant in the E-W striking shear zone. Additionally, the presence of mylonitic foliation and mineral stretching lineation (Figures 7B, C) indicated brittle-ductile shear deformation, primarily occurring within a horizontal NW-SE compression stress field (Figure 6D). The calcite-quartz veins (Figures 4M, 9J) and striation structures (Figures 4L, 9I) developed within the shear zone and its surrounding rocks indicate the superimposition of a later left-lateral normal faulting deformation. Moreover, the structural stress field inferred from the striations exhibited the characteristics of near-horizontal E-W compression. The deformation processes described above are generally consistent with the structural characteristics of the main E-W striking shear zones and veins in the Xiaoqinling area (Wang X. C. et al., 2012; Zhao et al., 2012; Tan et al., 2013; Yan et al., 2013). Furthermore, they aligned with the NW-SE compressive stress experienced by the main body of the E-W striking veins (Tan et al., 2013; Yan et al., 2013).

Within the E-W striking veins and shear deformation zones, there was also significant development of NE-striking veins (Figures 4, 5). The main orientation of these veins was trending to southeast with a dip angle of approximately 50°, and they were notably controlled by the left-lateral thrusting shear deformation zone (Figures 4B, 6I). Structural analysis of the NE-striking veins and their surrounding E-W striking veins revealed that the geometry, kinematics, and dynamics of the two sets of veins or shear zones were significantly different; the NE-striking shear zone or veins offset the E-W striking veins (Figure 6), and the E-W striking veins had traction folding characteristics near the NE-striking veins at the intersection position, indicating that the regional left-lateral veins and shear zones offset the E-W striking veins and shear zones (Chen et al., 2021).

Additionally, the relationships between the early stage milky-white quartz veins and the shear zone indicated that these veins may have formed during sinistral thrust deformation (D1) (Figures 4A, 9K), which may represent early deformation in the GSZ (Wang X. C. et al., 2012; Tan et al., 2013). Therefore, the E-W striking shear zone was mainly controlled by dextral thrusting during the development of ore-bearing veins, which were overprinted on the early sinistral shear, followed by sinistral normal faulting associated with the development of calcite–quartz veins. The NE–SW-trending belt of sinistral deformation that cuts the E–W-trending shear zone may represent the most recent deformation in the Xiaoqinling area (Zhang et al., 2016; Chen et al., 2021).

5.2 Timing of the E-W striking shear zone

Owing to the uncertainty of the deformation characteristics during the main mineralization period, the timing of the E-W striking mineralization of the Xiaoqinling gold deposits has been debated.

Recently, molybdenite Re–Os and Ar–Ar ages have been obtained from alteration-related minerals in the Xiaoqinling area, with results concentrated in the Late Triassic (233–206 Ma) mainly in the Dahu gold deposit (Li et al., 2007; Li et al., 2008; Jiang et al., 2009; Li et al., 2011; Jian et al., 2015) and Late Jurassic–Early Cretaceous (143–120 Ma) (Li et al., 2002; Wang et al., 2002; Li et al., 2007). The quartz-vein-hosted copper deposit in the Xiong'er area yielded a Re–Os age of 230 ± 31 Ma, which is coeval with early Mesozoic mineralization in the region (Deng and Wang, 2016; Cao et al., 2017). The latest research on structural deformation has also obtained the Late Triassic deformation age within the Xiaoqinling (Li et al., 2020) and Late Triassic magmatic activity in the Huashan pluton (Hu et al., 2012), indicating the development of Late Triassic deformation in the Xiaoqinling area. However, an accurate definition of the deformation time of the E-W striking shear zone in the southern region is still lacking.

Seven molybdenite samples collected from the Q539 located at western segment of GSZ defined a well-constrained isochron age of 230.2 ± 2.6 Ma (Figure 10). All of the molybdenite samples developed along the NE-striking and S-trending structural foliation, which were resulted by the thrust deformation (Figure 8). In addition, the Sheet-like molybdenite parallel to the structural planes, indicating that its formation is synchronous with E-W striking dextral thrust deformation. This age was consistent with the molybdenite Re-Os isotope ages from the Huanchiyu Shear

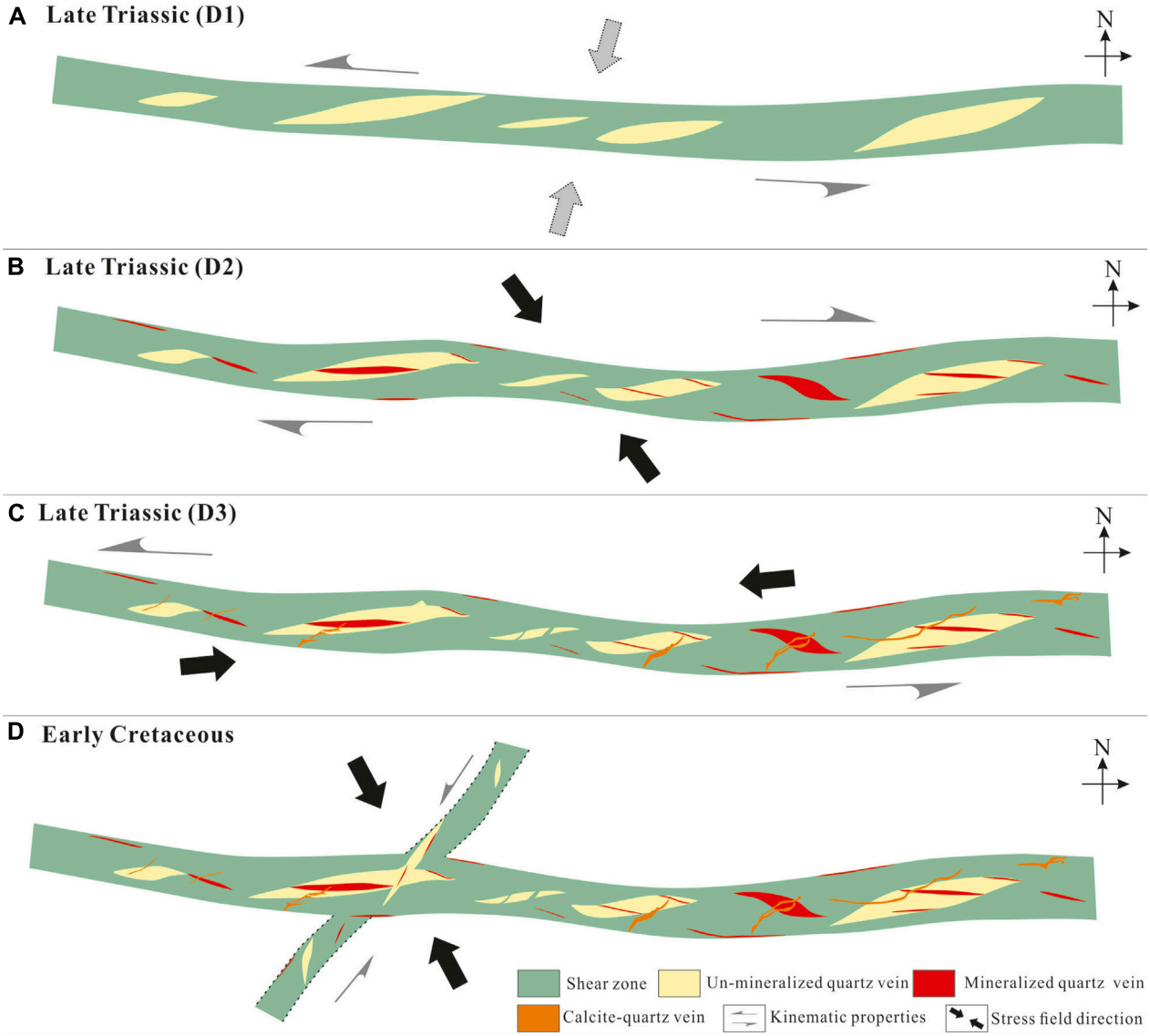

FIGURE 11
Structural model of mineralization mechanism for E-W striking shear zone in Xiaoqinling area. **(A)** Sinistral thrust deformation in Late Triassic; **(B)** Dextral thrust deformation in Late Triassic; **(C)** Sinistral normal faulting deformation in Late Triassic; **(D)** NE-SW striking shear zone overprinted on the E-W striking shear zone in Early Cretaceous.

zone, which is parallel to the GSZ and developed in the northern part of the Xiaoqinling area (Li et al., 2007; Li et al., 2008; Jiang et al., 2009; Li et al., 2011; Jian et al., 2015). Moreover, a large number of E-W striking ore veins, F5, were also developed in the Huanchiyu Shear zone (Figure 1), indicating that the formation of the E-W striking shear zone and molybdenite was contemporaneous and that the shear zone was formed in the Late Triassic.

Unlike the Late Triassic age, a large number of late Mesozoic Ar-Ar ages were also obtained within the GSZ, such as 146–128 Ma in Q507 (Xu Q. D. et al., 1998; Li et al., 2002; Li et al., 2012a), 144–119 Ma in Q8 (Li et al., 2012a), 130–129 Ma in Q875 (Wang et al., 2002), and 135–124 Ma in S60 (Li et al., 2012b). These Ar–Ar ages are accompanied by the activity of granitic magma in the Xiaoqinling area (Mao et al., 2010; Hu et al., 2012; Zhao et al., 2012; Yang et al., 2020), which may represent the superimposed deformation of the E-W striking shear zone during late Mesozoic tectono-thermal events (Jiang et al., 2009).

5.3 Mineralization mechanism of E-W striking shear zone

From the Late Jurassic to Early Cretaceous, the Xiaoqinling area experienced intense granitic magmatic activity (Mao et al., 2010; Hu et al., 2012; Zhao et al., 2012; Yang et al., 2020), which was associated with the large-scale mineralization during the late Mesozoic in the North China Block (Zhu et al., 2015; Deng and Wang, 2016). Consequently, it is believed that the main ore-forming period for

gold deposits in the Xiaoqinling region occurred during the late Mesozoic. These deposits are classified as magmatic-hydrothermal (or Jiaodong-type) deposits formed in an extensional environment resulting from lithospheric thinning in the North China Block (Mao et al., 2005; Li et al., 2012a; Li et al., 2012b; Deng and Wang, 2016; He et al., 2016).

However, fluid inclusions are composed of CO_2-H_2O-NaCl±CH_4 system with medium to low salinity, and the mineralization temperature is medium to high temperature (225°C–407°C), indicating the existence of metamorphic hydrothermal from deep sources (Chen et al., 1998; Fan et al., 2000; Qi et al., 2002; Jiang et al., 2009; Zhao et al., 2011; Zhou et al., 2014; Zhou et al., 2015). The magmatic-hydrothermal model cannot fully explain the widespread presence of metamorphic-hydrothermal material composition in the region. In contrast, the Late Triassic mineralization aligns well with the collision and orogeny processes between the North China and Yangtze blocks. Moreover, there is no evidence of large-scale early Mesozoic magmatic activity over the entire Xiaoqinling area (Hu et al., 2012). Consequently, it is believed that Late Triassic mineralization in the region was associated with orogenic-type gold deposits related to collisions between tectonic plates during the early Mesozoic (Chen et al., 2004; Chen et al., 2005; Jiang et al., 2009; Pirajno, 2009; Chen, 2010; Zhao et al., 2011; Zhou et al., 2015; Cao et al., 2017).

The E–W-striking shear zone was overprinted by the late NE-trending shear zone, and the structural characteristics of the mineralized material suggest that three phases of deformation and mineralization occurred in the E–W-striking shear zone in the Xiaoqinling area, with a metallogenic period in the Late Triassic followed by superimposed mineralization in the Early Cretaceous (Figure 11).

During the Late Triassic, the Xiaoqinling area underwent E–W-striking sinistral thrust deformation. The development of an E–W-trending shear zone formed a confined space, where the upward migration of ore-forming fluids along the fractures resulted in the development of milky-white, unmineralized quartz veins (Figure 11A). This early sinistral thrust deformation characteristic is consistent with the sinistral transpression in the Longmenshan (Yan et al., 2018a; Yan et al., 2018b), Mianlue (Li et al., 2007; Chen et al., 2010), and Dongjiangkou (Li Y. et al., 2019) areas, which is associated with the oblique subduction of the Yangtze Block beneath the North China Block (Li et al., 2019). Subsequently, accompanied by a change in the stress field, the shear zone underwent dextral thrust deformation and formed numerous ore-bearing quartz veins (Figure 11B). The sinistral normal faulting deformation developed with the stress field transformation, which was associated with the formation of calcite-quartz veins (Figure 11C). The stress field transformation of the E–W-striking shear zone in the Xiaoqinling area was related to the N–S collision between the North China and Yangtze blocks during the early Mesozoic (Ratschbacher et al., 2003; Zhang et al., 2004; Chen et al., 2006; Chen et al., 2008; Dong et al., 2011; Meng and Zhang, 2014; Dong et al., 2016), as well as the injection of hydrothermal fluids. However, there is still a lack of evidence regarding the timing of the three phases of deformation.

During Early Cretaceous, the Pacific plate subducted beneath the Eurasian plate (Zhu et al., 2015; Deng and Wang, 2016; Li S. et al., 2019). The North China Block underwent a large-scale extension that gradually influenced the Xiaoqinling area (Wang T. et al., 2012). The intrusion of granite provides a heat source (Mao et al., 2010; Hu et al., 2012; Zhao et al., 2012), increases the activity of ore-bearing fluid, and provides the driving force for the reactivation, migration, and enrichment of Au and Mo in this region (Li et al., 1998; Li et al., 2007). NE–SW-striking ore-bearing quartz veins may also have been overprinted in the early E-W striking shear zone during this period (Figure 11D).

6 Conclusion

(1) The E-W striking shear zone in Xiaoqinling was mainly controlled by dextral thrusting during the development of ore-bearing veins, which were overprinted on early sinistral shearing, followed by sinistral normal faulting associated with the development of calcite–quartz veins.
(2) Seven molybdenite samples defined an isochron age of 230.2 ± 2.6 Ma, representing that the E-W striking shear zone was formed in the Late Triassic.
(3) The E–W-striking shear zone is overprinted by the NE-trending shear zone, which represents the main orogenic metallogenic period in the Late Triassic superimposed by magmatic hydrothermal mineralization in the Early Cretaceous.

Data availability statement

The original contributions presented in the study are included in the article/supplementary material, further inquiries can be directed to the corresponding author.

Author contributions

HC: Conceptualization, Data curation, Funding acquisition, Investigation, Project administration, Supervision, Writing–original draft, Writing–review and editing. G-FZ: Data curation, Investigation, Writing–original draft. HB: Project administration, Resources, Writing–review and editing. G-SC: Resources, Writing–review and editing. H-HZ: Data curation, Investigation, Resources, Writing–review and editing. P-JM: Investigation, Writing–review and editing. Y-JJ: Data curation, Writing–review and editing.

Funding

The author(s) declare financial support was received for the research, authorship, and/or publication of this article. This research was funded by the National Natural Science Foundation of China (41772217) and the Geological Investigation Project of China Geological Survey (12120114014101).

Acknowledgments

We thank Geological Team No. 6 of the Shaanxi Bureau of Geology and Mineral Resources and Guo Long of the Chen'er gold

deposit for help during fieldwork. We greatly appreciate the work of reviewers who provided constructive and detailed reviews and suggestions to improve the manuscript.

Conflict of interest

Author G-SC was employed by Shaanxi Xinyuan Limited by Share Ltd.

The remaining authors declare that the research was conducted in the absence of any commercial or financial relationships that could be construed as a potential conflict of interest.

The reviewer LQ declared a shared affiliation with the author P-JM to the handling editor at the time of review.

Publisher's note

References

Cao, M. P., Yao, J. M., Deng, X. H., Yang, F. Y., Mao, G. Z., and Mathur, R. (2017). Diverse and multistage Mo, Au, Ag–Pb–Zn and Cu deposits in the xiong'er terrane, east qinling: from triassic Cu mineralization. *Ore Geol. Rev.* 81, 565–574. doi:10.1016/j.oregeorev.2016.02.014

Chao, Y. (1989). The metallogenetic epoch of the Xiaoqinling gold deposit. *Northwest. Geol.* 7, 52–55. (in Chinese with English abstract).

Chen, H., Hu, J. M., Wu, G. L., and Gao, W. (2010). Study on the intracontinental deformation of the Mian-Lue suture belt, western Qinling. *Acta Pet. Sin.* 26 (4), 1277–1288. doi:10.1046/j.1365-2958.2000.01819.x

Chen, H., Mu, P. J., Zhang, H. H., Zhu, G. F., Dong, H. Y., and Wang, H. H. (2021). Structural deformation and mineralization of NNE-striking veins in xiaoqinling area, Central China. *J. Earth Sci. Environ.* 43 (2), 291–314. doi:10.19814/j.jese.2021.01031

Chen, Y. J. (2010). Indosinian tectonic setting, magmatism and metallogenesis in Qinling Orogen, central China. *Geol. China* 37, 854–865. doi:10.3969/j.issn.1000-3657.2010.04.003

Chen, Y. J., Li, X., Qin, S., Gao, X. L., and Zhang, J. G. (1998). Study on ore-bearing fluid and its implication for fluid action in collisional orogenic system of shanggong gold deposit in henan provinc. *Prog. Nat. Sci.* 8 (1), 75–78. (in Chinese with English abstract).

Chen, Y. J., Pirajno, F., Li, N., Guo, D. S., and Lai, Y. (2009). Isotope systematics and fluid inclusion studies of the Qiyugou breccia pipe-hosted gold deposit, Qinling Orogen, Henan province, China: implications for ore genesis. *Ore Geol. Rev.* 35, 245–261. doi:10.1016/j.oregeorev.2008.11.003

Chen, Y. J., Pirajno, F., and Qi, J. P. (2005). Origin of gold metallogeny and sources of ore-forming fluids, Jiaodong province, eastern China. *Int. Geol. Rev.* 47, 530–549. doi:10.2747/0020-6814.47.5.530

Chen, Y. J., Pirajno, F., and Qi, J. P. (2008). The Shanggong gold deposit, eastern Qinling Orogen, China: isotope geochemistry and implications for ore genesis. *J. Asian Earth Sci.* 33, 252–266. doi:10.1016/j.jseaes.2007.12.002

Chen, Y. J., Pirajno, F., Qi, J. P., Li, J., and Wang, H. H. (2006). Ore geology, fluid geochemistry andgenesis of the Shanggong gold deposit, eastern Qinling Orogen, China. *Resour. Geol.* 56, 99–116. doi:10.1111/j.1751-3928.2006.tb00272.x

Chen, Y. J., Pirajno, F., and Sui, Y. H. (2004). Isotope geochemistry of the Tieluping silver-lead deposit, Henan, China: a case study of orogenic silver-dominated deposits and related tectonic setting. *Miner. Deposita* 39, 560–575. doi:10.1007/s00126-004-0429-9

Deng, J., and Wang, Q. F. (2016). Gold mineralization in China: metallogenic provinces, deposit types and tectonic framework. *Gondwana Res.* 36, 219–274. doi:10.1016/j.gr.2015.10.003

Dong, Y. P., and Santosh, M. (2016). Tectonic architecture and multiple orogeny of the qinling orogenic belt, Central China. *Gondwana Res.* 29, 1–40. doi:10.1016/j.gr.2015.06.009

Dong, Y. P., Yang, Z., Liu, X. M., Sun, S. S., Li, W., Cheng, B., et al. (2016). Mesozoic intracontinental orogeny in the qinling Mountains, central China. *Gondwana Res.* 30, 144–158. doi:10.1016/j.gr.2015.05.004

Dong, Y. P., Zhang, G. W., Neubauer, F., Liu, X. M., Genser, J., and Hauzenberger, C. (2011). Tectonic evolution of the Qinling orogen, China. Review and synthesis. *J. Asian Earth Sci.* 41, 213–237. doi:10.1016/j.jseaes.2011.03.002

Du, A. D., Wu, S. Q., Sun, D. Z., Wang, S. X., Qu, W. J., Richard, M. H. S., et al. (2004). Preparation and certification of Re-Os dating reference materials: molybdenites HLP and JDC. *Geostand. Geoanalytical Res.* 28 (1), 41–52. doi:10.1111/j.1751-908x.2004.tb01042.x

Fan, H. R., Xie, Y. H., Zhai, M. G., and Jin, C. W. (2003). A three stage fluid flow model for Xiaoqinling lode gold metallogenesis in the He'nan and Shannxi provinces, central China. *Acta Petrol. Sin.* 19, 260–266. doi:10.3969/j.issn.1000-0569.2003.02.007

Fan, H. R., Xie, Y. H., Zhao, R., and Wang, Y. L. (2000). Dual origins of Xiaoqinling gold-bearing quartz veins: fluid inclusion evidence. *Chin. Sci. Bull.* 45, 1424–1430. doi:10.1007/BF02886252

Fang, W. X., Li, Y. L., and Huang, Z. Y. (2000). On dynamics if metallogenic geochemistry for gold deposits in the Xiaoqinling area. *Geotect. Metallogenia* 24, 155–162. doi:10.3969/j.issn.1001-1552.2000.02.008

Feng, J. Z. (2009). Ore-controlling structure and model in Xiaoqinling gold deposit, Henan. *Mineral Resour. Geol.* 23, 302–307. doi:10.3969/j.issn.1001-5663.2009.04.003

Han, F., Bai, H., Wang, H. P., Wen, Y. G., Zhang, H. H., and Han, X. (2016). The characteristics of ore controlling structure and deep mineralization prognosis of the Q240 vein in Xiaoqinling gold field. *J. Geomechanics* 22, 232–244. doi:10.3969/j.issn.1006-6616.2016.02.005

Hao, H. D., Cao, Y., Sheng, T., and Zong, Z. J. (2020). Geochronology, petrogenesis and oxidation state of the Wenyu igneous suite in the xiaoqinling district, north China craton: implications for lithospheric thinning and magma fertility. *Lithos* 370-371, 105646. doi:10.1016/j.lithos.2020.105646

He, C. S., Santosh, M., and Yang, Q. Y. (2016). Gold metallogeny associated with craton destruction: a geophysical perspective from the North China Craton. *Ore Geol. Rev.* 75, 29–41. doi:10.1016/j.oregeorev.2015.12.004

Hu, G. H., Zhao, T. P., Zhou, Y. Y., and Wang, S. Y. (2013). Meso-Neoproterozoic sedimentary formation in the southern margin of the North China Craton and its geological implications. *Acta Petrol. Sin.* 29, 2491–2507. doi:10.1002/ppp.1771

Hu, J., Jiang, S. Y., Zhao, H. X., Shao, Y., Zhang, Z. Z., Xiao, E., et al. (2012). Geochemistry and petrogenesis of the Huashan granites and their implications for the Mesozoic tectonic settings in the Xiaoqinling gold mineralization belt, NW China. *J. Asian Earth Sci.* 56, 276–289. doi:10.1016/j.jseaes.2012.05.016

Hu, S., Raza, A., Kohn, B. P., Reiners, P. W., Ketcham, R. A., Wang, J., et al. (2006). Late Mesozoic and Cenozoic thermotectonic evolution along a transect from the north China craton through the Qinling orogen into the Yangtze craton, central China. *Tectonics* 25 (6), 1029–1044. doi:10.1029/2006TC001985

Jia, X. L., Zhu, X. Y., Zhai, Y. Z., Zhang, H., Wu, J. L., Liu, T., et al. (2016). Late Mesoarchean crust growth event: evidence from the ca. 2.8 Ga granodioritic gneisses of the Xiaoqinling area, southern North China Craton. *Earth Sci.* 61, 974–990. doi:10.1007/s11434-016-1094-y

Jian, W., Lehmann, B., Mao, J. W., Ye, H. S., Li, Z. Y., He, H. J., et al. (2015). Mineralogy, fluid characteristics, and Re-Os age of the late triassic Dahu Au-Mo deposit, xiaoqinling region, Central China: evidence for a magmatic-hydrothermal origin. *Econ. Geol.* 110, 119–145. doi:10.2113/econgeo.110.1.119

Jiang, N. (2000). Hydrothermal fluid evolution associated with gold mineralization at the Wenyu mine, xiaoqinling district, China. *Resour. Geol.* 50, 103–112. doi:10.1111/j.1751-3928.2000.tb00060.x

Jiang, S. Y., Dai, B. Z., Jiang, Y. H., Zhao, H. X., and Hou, M. L. (2009). Jiaodong and Xiaoqinling: two orogenic gold provinces formed in different tectonic setting. *Acta Petrol. Sin.* 25 (11), 2727–2738. doi:10.1016/j.sedgeo.2009.09.007

Leng, C. B., Zhang, X. C., Zhong, H., Hu, R. Z., Wei, D. Z., and Li, C. (2013). Re–Os molybdenite ages and zircon Hf isotopes of the Gangjiang porphyry Cu–Mo deposit in the Tibetan Orogen. *Miner. Deposita* 48, 585–602. doi:10.1007/s00126-012-0448-x

Li, H. M., Ye, H. T., Mao, J. W., Wang, D. H., Chen, Y. C., and Du, A. D. (2007). Re-Os dating of molybdenites from Au(-Mo)deposits in Xiaoqinling gold ore district and its geological significance. *Mineral. Deposits* 26, 417–424. doi:10.3969/j.issn.0258-7106.2007.04.005

Li, J. W., Bi, S. J., Selby, D., Chen, L., Vasconcelos, P., Thiede, D., et al. (2012a). Giant mesozoic gold provinces related to the destruction of the North China craton. *Earth Planet. Sci. Lett.* 349-350, 26–37. doi:10.1016/j.epsl.2012.06.058

Li, J. W., Li, Z. K., Zhou, M. F., Chen, L., Bi, S. J., Deng, X. D., et al. (2012b). The early cretaceous yangzhaiyu lode gold deposit, north China craton: a link between craton reactivation and gold veining. *Econ. Geol.* 107, 43–79. doi:10.2113/econgeo.107.1.43

Li, N., Chen, Y. J., Fletcher, I. R., and Zeng, Q. T. (2011). Triassic mineralization with Cretaceous overprint in the Dahu Au–Mo deposit, Xiaoqinling gold province: constraints from SHRIMP monazite U–Th–Pb geochronology. *Gondwana Res.* 20, 543–552. doi:10.1016/j.gr.2010.12.013

Li, N., Sun, Y. L., Xue, L. W., and Li, W. B. (2008). Molybdenite Re-Os isotope age of the Dahu Au-Mo deposit, Xiaoqinling and the Indosinian minerallzation. *Acta Petrol. Sin.* 24, 810–816.

Li, Q. Z., Chen, Y. J., Zhong, Z. Q., Li, W. L., Li, S. R., Guo, X. D., et al. (2002). Ar-Ar dating on the metallogenesis of the dongchuang gold deposit in the xiaoqinling area. *Acta Geol. Sin.* 76, 488–493. doi:10.1111/j.1755-6724.2002.tb00102.x

Li, S., Kusky, T. M., Wang, L., Zhang, G., Lai, S., Liu, X., et al. (2007). Collision leading to multiple-stage large-scale extrusion in the Qinling orogen: insights from the Mianlue suture. *Gondwana Res.* 12 (1-2), 121–143. doi:10.1016/j.gr.2006.11.011

Li, S., Suo, Y., Li, X., Zhou, J., Santosh, M., Wang, P., et al. (2019b). Mesozoic tectono-magmatic response in the east asian ocean-continent connection zone to subduction of the paleo-pacific plate. *Earth-Science Rev.* 192, 91–137. doi:10.1016/j.earscirev.2019.03.003

Li, S. R., Li, Q. Z., Li, W. L., and Guo, X. D. (1998). A new viewpoint of ore genesis in Xiaoqinling gold field. *Gold Geol.* 4, 41–49. (in Chinese with English abstract).

Li, Y., Li, S. Z., Liang, W. T., Lu, R. K., Zhang, Y. J., Li, X. Y., et al. (2019a). Incremental emplacement and syn-tectonic deformation of Late Triassic granites in the Qinling Orogen: structural and geochronological constraints. *Gondwana Res.* 72, 194–212. doi:10.1016/j.gr.2019.04.001

Li, Y. J., Zhu, G., Gu, C. C., Liu, C., Zhang, S., Zhao, T., et al. (2020). The xiaoqinling metamorphic core complex: a record of early cretaceous backarc extension along the southern part of the North China craton. *Geol. Soc. Am. Bull.* 132 (3-4), 617–637. doi:10.1130/B35261.1

Liu, Y. H., Qi, X. S., Li, Z. H., Luo, G. G., Zhao, D. H., An, J., et al. (2015). Geological characteristics and genesis of Chen'er gold deposit in Shaanxi province. *Northwest. Geol.* 48, 186–195. doi:10.3969/j.issn.1009-6248.2015.02.019

Lu, X. X., Li, M. L., Wang, W., Yu, Z. P., and Shi, Y. Z. (2008). Indosinian movement and metallogenesis in Qinling orogenic belt. *Mineral. Deposits* 27, 762–773. doi:10.3969/j.issn.0258-7106.2008.06.009

Ludwig, K. R. (2011). *User's manual for isoplot/ex Version4.15: a geochronological toolkit for microsoft excel*. Berkeley: Berkeley Geochronology Center.

Luo, B. J., Zhang, H. F., Zhang, L. Q., Zhang, C., Shen, L. M., Xiao, Z. Q., et al. (2020). The magma plumbing system of Mesozoic Shanyang porphyry groups, South Qinling and implications for porphyry copper mineralization. *Earth Planet. Sci. Lett.* 543, 116346. doi:10.1016/j.epsl.2020.116346

Mao, J. W., Goldfarb, R. J., Zhang, Z. W., Xu, W. Y., Qiu, Y. M., and Deng, J. (2002). Gold deposits in the xiaoqinling–xiong'ershan region, qinling Mountains, central China. *Min. Deposita* 37, 306–325. doi:10.1007/s00126-001-0248-1

Mao, J. W., Xie, G. Q., Pirajno, F., Ye, H. S., Wang, Y. B., Li, Y. F., et al. (2010). Late Jurassic–Early Cretaceous granitoid magmatism in Eastern Qinling, central-eastern China: SHRIMP zircon U–Pb ages and tectonic implications. *Aust. J. Earth Sci.* 57, 51–78. doi:10.1080/08120090903416203

Mao, J. W., Xie, G. Q., Zhang, Z. H., Li, X. F., Wang, Y. T., Zhang, C. Q., et al. (2005). Mesozoic large-scale metallogenic pulses in north China and corresponding geodynamic settings. *Acta Petrol. Sin.* 21 (1), 169–188. doi:10.3321/j.issn:1000-0569.2005.01.017

Meng, Q. R., and Zhang, G. W. (2014). Geologic framework and tectonic evolution of the Qinling orogen, central China. *Tectonophysics* 323, 183–196. doi:10.1016/S0040-1951(00)00106-2

Pirajno, F. (2009). *Hydrothermal processes and mineral systems*. Perth: Springer.

Qi, J. P., Chen, Y. J., and Li, Q. Z. (2002). Synthesis of hydrothermal metallogenesis in xiaoqinling orogenic gold field. *Mineral. Deposits* 21 (Z6), 1009–1012. (in Chinese with English abstract).

Qiang, S. F., Bi, S. J., Deng, X. D., Guo, L. Q., and Li, J. W. (2013). Monazite U-Th-Pb ages of the qinnan gold deposit, xiaoqinling district: implications for regional metallogenesis and tectonic setting. *Earth Sci.* 38 (1), 43–56. doi:10.3799/dqkx.2013.005

Ratschbacher, L., Hacker, B. R., Calvert, A., Webb, L. E., Grimmer, J. C., McWilliams, M. O., et al. (2003). Tectonics of the Qinling (central China): tectonostratigraphy, geochronology, and deformation history. *Tectonophysics* 366, 1–53. doi:10.1016/S0040-1951(03)00053-2

Smoliar, M. I., Walker, R. J., and Morgan, J. W. (1996). Re-Os ages of group IIA, IIIA, IVA, and IVB iron meteorites. *Science* 271, 1099–1102. doi:10.1126/science.271.5252.1099

Tan, M. T., Yao, S. Z., Ding, Z. J., Zhou, Z. G., and He, M. C. (2014). Trend surface analysis of main ore veins with applications in mineral resources prediction in Xiaoqinling gold ore field. *Earth Sci.* 39, 303–311. doi:10.3799/dqkx.2014.029

Tan, M. T., Yao, S. Z., He, M. C., and Ding, Z. J. (2013). Structural controls on gold mineralization and itsimplications in ore prospecting for the Dongchuang gold deposit in the Xiaoqinling district. *Geotect. Metallogenia* 37, 225–234. doi:10.3969/j.issn.1001-1552.2013.02.006

Tan, X. H., Wang, L., and Wang, R. T. (2012). Study on mineral exploration in depth of Xiaoqinling gold deposit region-a case of Chen'er gold ore deposit. *Northwest. Geol.* 45, 72–80. doi:10.3969/j.issn.1009-6248.2012.03.010

Wang, H. H., Chen, H., Chen, L. Y., Bai, H., and Zhang, H. H. (2023). Protracted Paleoproterozoic partial melting recorded in the Taihua Complex, southern North China Craton: insights from zircon U–Pb ages of leucosomes within migmatites. *J. Asian Earth Sci.* 243, 105523. doi:10.1016/j.jseaes.2022.105523

Wang, J. D., Wang, D. Z., Zhan, X. F., Wei, J. H., Xiao, H., Li, H., et al. (2018). Structural controls on mineralization and distribution of orebodies in the southern ore belt of the xiaoqinling district. *Geotect. Metallogenia* 42 (6), 1064–1077. doi:10.16539/j.ddgzyckx.2018.06.009

Wang, T., Guo, L., Zheng, Y., Donskaya, T., Gladkochub, D., Zeng, L., et al. (2012a). Timing and processes of late mesozoic mid-lower-crustal extension in continental NE asia and implications for the tectonic setting of the destruction of the North China craton: mainly constrained by zircon U–Pb ages from metamorphic core complexes. *Lithos* 154, 315–345. doi:10.1016/j.lithos.2012.07.020

Wang, T. H., Mao, J. W., and Wang, Y. B. (2008). Reasearch on SHRIMP U-Pb chronology in Xiaoqinling-Xionger' Shan area: the evidence of delamination of lithosphere in Qinling orogenic belt. *Acta Petrol. Sin.* 24, 1273–1287. doi:10.1007/BF02919155

Wang, X. C., Niu, S. Y., Cui, X. X., Yan, J. S., Feng, J. Z., Sun, W. Z., et al. (2012b). Geological and structural characteristics of the S507 gold vein group in the Dongchuang gold deposit, Xiaoqinling, China. *Geotect. Metallogenia* 36, 541–548. doi:10.3969/j.issn.1001-1552.2012.04.008

Wang, Y. T., Mao, J. W., Lu, X. X., and Ye, A. W. (2002). The ^{40}Ar-^{39}Ar age and its significance of deep-seated mineralized alteration rocks in the Q875 vein, Xiaoqinling gold deposit, Henan Province. *Chin. Sci. Bull.* 47, 1427–1431. doi:10.3321/j.issn:0023-074X.2002.18.015

Wang, Y. T., Ye, H. S., Ye, A. W., Liu, S. L., Hao, J. L., Liu, J. C., et al. (2020). Cooling and uplift history of the Niangniangshan granitic pluton in the Xiaoqinling goldfield, central China: implications for tectonic evolution and gold mineralization. *Geol. J.* 55 (8), 5967–5977. doi:10.1002/gj.3662

Wen, Z. H., Li, L., Li, S. L., Santosh, M., Liu, J., Yuan, M., et al. (2020). Gold-forming potential of the granitic plutons in the xiaoqinling gold province, southern margin of the North China craton: perspectives from zircon U–Pb isotopes and geochemistry. *Geol. J.* 55 (8), 5725–5744. doi:10.1002/gj.3619

Wu, X. G., Xu, J. H., Wei, H., Lin, L. H., Zhang, G. R., Hui, D. F., et al. (2012). A study of fluid inclusions of Dongtongyu gold deposit in Xiaoqinling area. *Mineral. Deposits* 31, 195–206. doi:10.3969/j.issn.0258-7106.2012.02.002

Xiong, X., Zhu, L. M., Zhang, G. W., Guo, A. L., Zheng, J., and Jiang, H. (2019). Origin of the Xiaohekou skarn copper deposit and related granitoids in the Zha-Shan ore cluster area, South Qinling, China. *Ore Geol. Rev.* 114, 103143. doi:10.1016/j.oregeorev.2019.103143

Xu, J. H., Lin, L. H., Wei, H., Wu, X. G., and Xian, D. F. (2013). Fluid inclusion study on the dongtongyu gold deposit in xiaoqinling Mt area, China. *Acta Geol. Sin. Engl. Ed.* 87, 808–810. doi:10.1007/s001260050192

Xu, J. H., Xie, Y. L., Jiang, N., and Bie, F. L. (1998a). Mineralogical, fluid inclusion, and stable isotope study of Wenyu-Dongchuang gold deposits in the Xiaoqinling Mt. area, west Henan, China. *Explor. Min. Geol.* 7, 321–332.

Xu, Q. D., Zhong, Z. Q., Zhou, H. W., Yang, F. C., and Tang, X. C. (1998b). 40Ar/39Ar dating of the Xiaoqinling gold area in Henan Province. *Geol. Rev.* 44, 323–327. (in Chinese with English abstract).

Yan, D. P., Qiu, L., Wells, M. L., Zhou, M. F., Meng, X., Lu, S., et al. (2018). Structural and geochronological constraints on the early Mesozoic north Longmen Shan Thrust Belt: foreland fold-thrust propagation of the SW Qinling orogenic belt, northeastern Tibetan plateau. *Tectonics* 37, 4595–4624. doi:10.1029/2018TC004986

Yan, D. P., Zhou, Y., Qiu, L., Wells, M. L., Mu, H. X., and Xu, C. G. (2018). The Longmenshan Tectonic Complex and adjacent tectonic units in the eastern margin of the Tibetan Plateau: a review. *J. Asian Earth Sci.* 164, 33–57. doi:10.1016/j.jseaes.2018.06.017

Yan, J. S., Niu, S. Y., Feng, J. Z., Sun, W. Z., Sun, A. Q., Wang, X. C., et al. (2013). An analysis of structural ore-controlling role in Xiaoqingling area. *Geol. China* 40, 538–548. doi:10.3969/j.issn.1000-3657.2013.02.018

Yang, Y. Z., Wang, Y., Siebel, W., Zhang, Y. S., and Chen, F. (2020). Zircon U-Pb-Hf, geochemical and Sr-Nd-Pb isotope systematics of late mesozoic granitoids in the lantian-xiaoqinling region: implications for tectonic setting and petrogenesis. *Lithos* 374-375, 105709. doi:10.1016/j.lithos.2020.105709

Zhang, C. L., Wang, T., and Wang, X. X. (2008). Origin and tectonic setting of the early mesozoic granitoids in qinling orogenic belt. *Geol. J. China Univ.* 14 (3), 304–316. (in Chinese with English abstract).

Zhang, G., Dong, Y., Lai, S., Guo, A., Meng, Q., Liu, S., et al. (2004). Mianle tectonic zone and Mianle suture zone on southern margin of Qinling-Dabie orogenic belt. *Sci. China Earth Sci.* 47 (4), 300–316. doi:10.1360/02YD0526

Zhang, H. H., Bai, H., Wang, H. P., Wen, Y. G., Han, F., Yang, Y. W., et al. (2016). Study on the Q173 vein in Xiaoqinling gold field with the method of structure-alteration-geochemistry prospecting prediction. *J. Geomechanics* 22, 270–284. doi:10.3969/j.issn.1006-6616.2016.02.008

Zhang, J. J., and Zheng, Y. (1999). Multistage extension and age dating of the Xiaoqinling metamorphic core complex, centeal China. *Acta Petrol. Sin.* 73, 139–147. doi:10.1111/j.1755-6724.1999.tb00821.x

Zhang, J. J., Zheng, Y. D., and Liu, S. W. (2000). Application of general shear theory to the study of formation mechanism of the metamorphic core complex: a case study of xiaoqinling in Central China. *Acta Geol. Sin.* 74, 19–28. doi:10.1111/j.1755-6724.2000.tb00428.x

Zhang, J. J., Zheng, Y. D., and Liu, S. W. (2003). Mesozoic tectonic evolution and ore-deposits formation in the gold mine field of Xiaoqinling. *Chin. J. Geol.* 38, 74–84. doi:10.3321/j.issn:0563-5020.2003.01.008

Zhang, K., Ren, H. W., Guo, G., Teng, F., and Wang, C. (2015). Tectonic development and ore-controling characteristics of Xiaoqinling gold field. *J. Geomechanics* 21, 415–425. doi:10.3969/j.issn.1006-6616.2015.03.012

Zhao, H. X., Frimmel, H. E., Jiang, S. Y., and Dai, B. Z. (2011). LA-ICP-MS trace element analysis of pyrite from the Xiaoqinling gold district, China: implications for ore genesis. *Ore Geol. Rev.* 43, 142–153. doi:10.1016/j.oregeorev.2011.07.006

Zhao, H. X., Jiang, S. Y., Frimmel, H. E., Dai, B. Z., and Ma, L. (2012). Geochemistry, geochronology and Sr–Nd–Hf isotopes of two Mesozoic granitoids in the Xiaoqinling gold district: implication for large-scale lithospheric thinning in the North China Craton. *Chem. Geol.* 294-295, 173–189. doi:10.1016/j.chemgeo.2011.11.030

Zhao, S. R., Li, J. W., Lentz, D., Bi, S. J., Zhao, X. F., and Tang, K. F. (2019). Discrete mineralization events at the hongtuling Au-(Mo) vein deposit in the xiaoqinling district, southern north China craton: evidence from monazite U-Pb and molybdenite Re-Os dating. *Ore Geol. Rev.* 109, 413–425. doi:10.1016/j.oregeorev.2019.04.025

Zhou, Z. J., Chen, Y. J., Jiang, S. Y., Hu, C. J., Yan, Q., and Zhao, H. X. (2015). Isotope and fluid inclusion geochemistry and genesis of the Qiangma gold deposit, Xiaoqinling gold field, Qinling Orogen, China. *Ore Geol. Rev.* 66, 47–64. doi:10.1016/j.oregeorev.2014.10.020

Zhou, Z. J., Chen, Y. J., Jiang, S. Y., Zhao, H. X., Qin, Y., and Hu, C. J. (2014). Geology, geochemistry and ore genesis of the Wenyu gold deposit, Xiaoqinling gold field, Qinling Orogen, southern margin of North China Craton. *Ore Geol. Rev.* 59, 1–20. doi:10.1016/j.oregeorev.2013.12.001

Zhu, R. X., Fan, H. R., Li, J. W., Meng, Q. R., Li, S. R., and Zeng, Q. D. (2015). Decratonic gold deposits. *Sci. China Earth Sci.* 58, 1523–1537. doi:10.1007/s11430-015-5139-x